Effects of magnetic field and La-for-Ce substitution in the $Ce_xLa_{1-x}NiGa_2$ series

تأثير المجال المغناطيسي و نسب ذرتي السيريوم و لانثانوم على مجموعة من الجزيئات المختلفة

A thesis submitted in partial fulfillment
of the requirements for the Masters degree
in Physics

Presented by

Maha Ali Zuod

Supervised by

Prof. Dr. Edward Sader

M.Sc.Thesis
Birzeit University
Palestine
2019

Effects of magnetic field and La-for-Ce substitution in the $Ce_xLa_{1-x}NiGa_2$ series

تأثير المجال المغناطيسي و نسب ذرتي السيريوم و لانثانوم على مجموعة من الجزيئات المختلفة

A thesis submitted in partial fulfillment
of the requirements for the Masters degree
in Physics

Presented by

Maha Ali Zuod

Supervised by

Prof. Dr. Edward Sader

M.Sc.Thesis
Birzeit University
Palestine
2019

BIRZEIT UNIVERSITY

Effects of magnetic field and La-for-Ce substitution in the $Ce_xLa_{1-x}NiGa_2$ series

تأثير المجال المغناطيسي و نسب ذرتي السيريوم و لانثانوم على مجموعة من الجزيئات المختلفة

by
Maha Zuod

This Thesis was defended successfully on September 18, 2019 and approved by

Committee Members		Signature and Date
Prof. Dr. Edward Sade	(Head Of Committee)	.....
Dr. Esmael Badran	(Internal Examiner)	.....
Dr. Hazem Abusara	(Internal Examiner)	.....

Birzeit University
2019

Declaration

I certify that this thesis, submitted for the degree of Master of Physics to the department of Physics at Birzeit University, is my own research except where otherwise acknowledged, and that this thesis (or any part of it) has not been submitted for a higher degree to any other university or institution.

Maha Zuod	Signature
June, 2019	.....

Acknowledgments

I would like to express my heartfelt gratitude and sincere appreciation to all people who greatly helped and supported me to accomplish this project. First and foremost, I would like to thank Prof. Dr. Joël Mesot for giving me the opportunity to join his research group. I am also genuinely grateful to Dr. Toni Shiroka for his professional guidance, constant encouragement, and valuable suggestions during the time of the thesis. I am also genuinely grateful to Dr. Nicolò Barbero who supervised this work, for his immense help, unfailing enthusiasm, and effective supervision at all times while carrying out this research work. He always provided detailed and constructive ideas that made the completion of this work successful. In addition, he was always accessible and willing to help me in all possible ways. I appreciate his patience and kindliness in explaining the concepts repeatedly.

A very special thanks to my first supervisor in Birzeit University Prof. Dr. Edward Sader for giving me the opportunity to do this thesis, as well as for his help, care and support. To Dr. Esmael Badran and Dr. Hazem Abusara for being part of the thesis defense.

Last but not least, I express my thanks and love to my husband Bahaaeddin Irziqat and everyone who directly and indirectly helped me to let this research work successfully. My deepest gratitude goes to my family for their unflagging love, advice, and support throughout my study, this dissertation would have been simply impossible without them. To them I dedicate this thesis.

I acknowledge that some data and figures are partially or completely reproduced from the internal report on the project authored by Dr. Nicolò Barbero .

Abstract

Nuclear magnetic resonance is a technique which is widely applied in solid state physics. It is sensible to the local fields present in the materials and, therefore, allows the investigation of their static and dynamic properties at microscopic scales. For instance, it gives access to the order parameter in an antiferromagnet. It is therefore a very suited tool for the study of complex microscopic physics as in the case of strongly-correlated systems.

In this work, we present the first microscopic studies, by nuclear magnetic resonance (NMR) of five new heavy-electron compounds, i.e. the $Ce_xLa_{1-x}NiGa_2$ series. The five x-values we chose to investigate are 0, 0.2, 0.5, 0.7 and 1, which show an antiferromagnetic (AF) phase transition for Ce level down to 50% below T_K involving small localized Ce moments. As probing nucleus, we have chosen ^{71}Ga, for consistency with the previous work [29] [30]. In particular we will present studies of the NMR shifts and lines-shapes and of the spin-lattice relaxation process for a wide range of temperatures, from 100 mK up to 300 K. In 5.003 T, the spin-lattice relaxation rate $T_1^{-1}(T)$ shows remarkable changes in its temperature dependence, highlighting a complex equilibrium among crystal-field, disorder-, Kondo-screening-, and RKKY interaction effects.

الملخص

الرنين المغناطيسي النووي هي تقنية تطبق على نطاق واسع في فيزياء الحالة الصلبة. حيث إنها حساسة للحقول المحلية الموجودة في المواد وبالتالي تسمح بالتحقيق في خصائصها الساكنة والديناميكية في المقاييس المجهرية. على سبيل المثال ، يمكنها منح حق الوصول إلى قياسات دقيقة في المواد ذات المغناطيسيه الحديدية المتضادة. لذلك فهي أداة مناسبة للغاية لدراسة الفيزياء المجهرية المعقدة لموادنا.

في هذا العمل ، نقدم أول دراسات مجهرية ، بواسطة الرنين المغناطيسي النووي لخمس مركبات جديدة ثقيلة الإلكترون، حيث تظهر جميعها مرحلة انتقالية لمضادات المغناطيسية عند درجات حرارة اقل من درجه حرارة نيل والتي تتضمن لحظات موضعية صغيرة مترجمة. لقد اخترنا ذره عنصر الجاليوم ذو العدد الذري ٧١ لدراسة الخصائص المغناطيسيه للمركبات من خلالها، ومقارنتها مع الاعمال السابقة . على وجه الخصوص ، سنقدم دراسات حول نوبات الرنين المغناطيسي النووي وأشكال الخطوط وعملية استرخاء الغزل الشبكي الدوار لمجموعة واسعة من درجات الحرارة تبدأ من ٠,٢ كيلفن الى ٣٠٠ كيلفن في مجال معناطيسي مقدارة ٥,٠٠٣ تسلا ، حيث يُظهر معدل استرخاء الشبكة الدورانية تغيرات ملحوظة في الاعتماد على درجة الحرارة.

Contents

List of Figures

List of Tables

Chapter 1

Interplay of Kondo effect and RKKY interaction

1.1 Crystal-field effects

The shapes of the atomic orbitals are different from one orbital to another (i.e. s orbitals have a spherical symmetry), so we need to know the shapes of the p, d and f orbitals to understand the effect of the surrounding environment on the energy level of an atom. Crystal-field theory is a model that explains the change in magnetic properties by describing the breaking of degeneracies of energy states by the effect of the surrounding charge distribution as a static electric field due to the crystal, usually d or f orbitals, in transition metal complexes in ionic crystal [1].

The crystal field is an electrostatic field derived from the surrounding ions and molecules (ligands). In transition metal compounds, the ligands are modeled as a negative charge attraction with the positively charged metal cation constituted by an electric dipole that repels electrons in the d-orbitals of the central metal ion due to repulsion between like charges [2]. The five degenerate d-orbital will lose their degeneracy where the effect of the electrons from the ligand will vary from d-orbitals to another. Thus that case has a splitting in energy level. For d-orbitals which have a strong-field ligands and weak-field ligands depending on how much is the splitting Δ of the d-orbital energy levels [3] . The electronic configuration of Ce^{3+} is [Xe]$4f^1$ with only one electron outside closed shells. The crystal field will split the energy levels into three doublets, [4, 5]

1.2 Kondo effect

Usually in pure metal the electrical resistance should decrease with a decrease in temperature that make the vibrations of the atoms small, furthermore the electrons can travel more easily through a metallic crystal, the resistivity of a conductor can be expressed as:

$$\rho = \rho_0 + aT^5 \tag{1.1}$$

where ρ_0 is the residual resistivity originating from lattice impurities, aT^5 comes from the lattice vibrations (phonons). In the 1930, they experimentally observed that

the electrical resistivity has a logarithmic decrease at low temperature in magnetic dilute alloys (diluted Kondo effect), which is also observed in many heavy fermion compounds with rare earth elements such as cerium (dense Knodo effect) [6]. This phenomenon explained by Kondo in 1964 so that it is called the Kondo effect where introduce a new formula for the resistivity:

$$\rho = \rho_0 + aT^5 + bT^2 - c_{\mathrm{m}} \ln \frac{\mu}{T} \tag{1.2}$$

where a, b, c_{m} are constants, aT^2 comes from the Fermi liquid properties and the last term derived by Kondo [7], as depicted in Fig. 1.1 .

The heavy fermion materials have two kinds of electrons, conduction electrons from outer orbitals, and electrons from inner f-orbitals called strongly correlated electrons. Kondo effect occurs when the localized magnetic moment $\vec{S}$ of the single magnetic impurity is interacted by the conduction electron density $\vec{s}(0)$ localized about the impurity, which is described by the Kondo Hamiltonian for $4f$ electronic states [8, 9].

$$\mathscr{H}_{\mathrm{K}} = -2J_{\mathrm{K}}\vec{S} \cdot \vec{s}(0) \tag{1.3}$$

The exchange coupling constant for the electron at the Fermi surface,

$$J_{\mathrm{K}} = V^2 \frac{U}{\varepsilon_f(\varepsilon_f + U)} \tag{1.4}$$

Where J_{K} is the interaction constant between the spins of the conduction electrons and the localized $4f$-electrons, V is the hybridization strength of the conduction band with the $4f$ states, ε_{f} is the energy of the localized $4f$ state and U is the on- site coulomb repulsion between electrons in the $4f$ shell. J_{K} is negative if ε_{f} is negative and $\varepsilon_{\mathrm{f}} + U$. The temperature for this interaction is the Kondo temperature T_{K} [10]:

$$T_{\mathrm{K}} = \left(\frac{D}{k_{\mathrm{B}}}\right) \exp\left(-\frac{1}{2J_{\mathrm{K}}N(E_{\mathrm{F}})}\right) \tag{1.5}$$

with D is the conduction electron band width and $N(E_{\mathrm{F}})$ is the single spin density of states at the Fermi level of the host. The effect of Kondo Hamiltonian $\mathscr{H}_{\mathrm{K}}$ in the dilute case is the following:

- $T \to 0$, a Kondo singlet state is formed when the impurity spin is completely screened by the conduction electrons.
- $T \gg T_{\mathrm{K}}$, the f-electrons are localized, as shown by the Curie Weiss behavior of the susceptibility.
- $T \approx T_{\mathrm{K}}$, the resistance shows a minimum with decreasing temperature until it saturate and increases logarithmically with further lowering of T

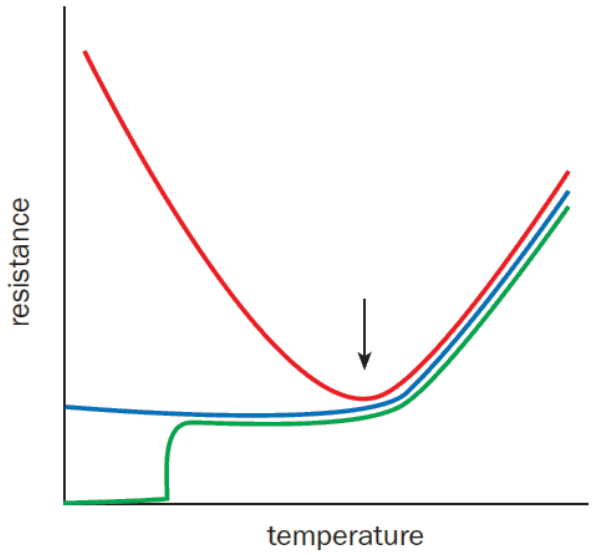

Figure 1.1: Resistivity at low temperatures, The blue line shows that for metal when the temperature is lowered, its resistance decreases towards a finite residual value.The green line shows the behavior of some metals which become superconducting at a critical temperature. However, the red line shows behavior of metals that contain magnetic impurities when taking the Kondo effect into account [11].

Periodic Anderson model

The above picture can be generalized in systems with periodical lattice of magnetic ions by Periodic Anderson model (PAM) [12]:

$$\mathscr{H}_{PAM} = \sum_{k,\sigma} \varepsilon(k) c^{\dagger}_{k\sigma} c_{k\sigma} + \sum_{k,\sigma} \varepsilon^{f}_{k} f^{\dagger}_{k\sigma} f_{k\sigma} - \sum_{k,\sigma} v_{k} \left(f^{\dagger}_{k\sigma} c_{k\sigma} + c^{\dagger}_{k\sigma} f_{k\sigma} \right) + U_{f} \sum_{j} n_{j\uparrow} n_{j\downarrow} \quad (1.6)$$

The first term describes the energy of the conduction electrons in the metal. the second term is the energy of the electrons on the impurity state. The third term describes the weak hybridization between the conduction band and the localized impurity electronic state, and the last term describes the on-site Coulomb repulsion within a f shell.

1.3 RKKY interaction

The indirect exchange interaction between nuclear spin and the conduction electrons was described by Ruderman, Kittel, Kasuya and Yoisda is therefore called RKKY interaction. As will describe in Sec. 2.2.1. If the distance between the rare earth atoms is too large to allow overlapping of the f-electrons wave functions, the direct interaction will be neglected by the systems, therefore the RKKY interaction become very important specially in metals containing rare-earth ions[13].The RKKY Hamiltonian is described by:

$$\mathscr{H}_{RKKY} = -\sum_{i \neq j} a_{ij} \vec{I}_{i} \cdot \vec{I}_{j} \quad (1.7)$$

with $\vec{I}_i$ the f-electron total angular momentum at the site i and

$$a_{ij} = -\frac{9N^2}{2E_F}\pi J_K^2(g_J-1)^2 F(2k_F r) \tag{1.8}$$

N is the number of conduction electrons per atom, g_J is the Landé g-factor of one localized spin, J_K is given by Eq. 1.4, E_F and k_F are the Fermi energy and the Fermi wave vector of the conduction electrons, respectively. The coupling can be ferromagnetic or antiferromagnetic depending on the sign of a_{ij}. The oscillatory function F(x) is given by:

$$F(x) = \frac{x\cos(x) - \sin(x)}{x^4} \tag{1.9}$$

The temperature for this interaction is the RKKY temperature T_{RKKY}

$$T_{RKKY} \propto N(E_F)J_K \tag{1.10}$$

1.4 Doniach's phase diagram

The Doniach's diagram describes the competition between the local Kondo effect, which is characterized by $T_K \sim \exp(-1/J_K)$ which tends to decrease the magnetic moment below T_K and the strength of the RKKY interactions which is characterized the magnetic order $T_{RKKY} \sim J_K^2$ below the Neél temperature (T_N) in cerium compounds.[3] [12]. The Doniach's diagram is illustrated in Fig.1.2 , which show the relation between several characteristic temperatures and the $J_K\rho$.In cerium compounds the competition occur between non-magnetic (Heavy fermion regime) and antiferromagnetism (AFM). For small values of J_K, T_N is larger than T_K and the system order magnetically (the RKKY interaction is dominant). In intermediate values of J_K magnetic order occurs with partially screened magnetic moment due to the Kondo effect, the Quantum Critical Point (QCP) at zero temperature in this regime separate between (AFM) phase and heavy fermi liquid phase. For large values of J_K, T_{RKKY} is smaller than T_K and the system tends to heavy fermion behavior [9].

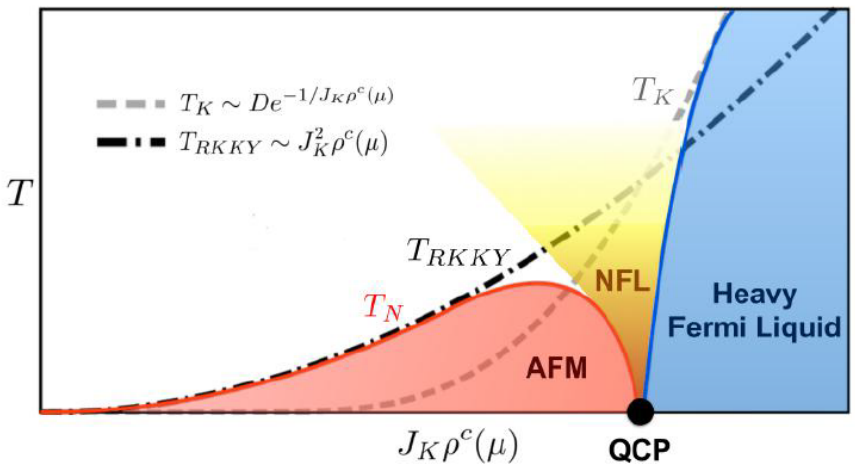

Figure 1.2: Doniach's phase diagram of a Kondo lattice [12]

1.5 Kondo disorder model

In dense heavy fermion compounds, instead of few diluted impurities, a regular lattice of magnetic impurities is found. As a consequence, the one-impurity model cannot describe the properties of their cerium compounds. In Sec. 1.2, we discussed how the heavy fermion materials have two kinds of electrons, where the f-electrons consider as a lattice of localized spins.The coupling between the conduction electrons and the strongly correlated electrons has been described by the Kondo lattice model.

The competition between the Kondo effect and the RKKY interaction is strongly affected by the disorder in alloys. This disorder can be studied by Kondo-disorder model if we consider the interaction between localized spins to be random (zero-mean distribution). A broad distribution of Kondo temperatures has been produced by the disorder, which is considered as the origin of the deviation of its properties from the Fermi-liquid behavior in heavy fermion compounds, such as cerium based, $CeNi_{1-x}Cu_x$ [14], or uranium based, $UCu_{5-x}Pd_x$ [15], compounds.

Chapter 2

NMR: theoretical aspects

2.1 Fundamentals of NMR

2.1.1 Nuclear magnetic resonance

The magnitude of the nuclear total angular momentum J is related to the spin quantum number I according to the relation:

$$J = \hbar\sqrt{I(I+1)}, \tag{2.1}$$

where $\hbar$ is the reduced Planck constant. If the external field is parallel to the z-direction, then the component of the nuclear spin angular momentum is:

$$J_z = I_z\hbar = m\hbar, \tag{2.2}$$

where I_z is the magnetic quantum number with multiplicity $2I+1$:

$$I_z \equiv m = -I, -I+1, ..., I-1, I. \tag{2.3}$$

In order to the NMR signal, the nucleus needs to have a non-zero nuclear spin. This condition is true when it contains an odd number of protons, neutrons, or both. Nuclei with an even number of both protons and neutrons have a nuclear spin equal to zero and, therefore, they are called NMR-inactive nuclei [16].
Nuclei with non-zero spin features a magnetic dipole moment $\mu = \gamma\hbar I$. We focus our attention on these nuclei in a static applied magnetic field B described by the Zeeman Hamiltonian:

$$\mathscr{H}_Z = -\mu \cdot B = -\gamma\hbar I \cdot B \tag{2.4}$$

Where γ is the magnetogyric ratio of the nuclear spin. The quantized axis is defined parallel to the external magnetic field, which is chosen to point along the z-axis, that is $B = B\hat{z}$. The effect of the external magnetic field is to lift the $(2I+1)$ fold degeneracy of the ground state in equally spaced energy level [17].

$$E_m = -m\hbar\gamma B \tag{2.5}$$

The difference in energy between two adjacent levels is defined as the Larmor frequency ($\nu_L = \omega_L/2\pi$)

$$\omega_L = \gamma B \tag{2.6}$$

The heart of the principle of nuclear magnetic resonance resides in the capability of inducing a transition between two Zeeman split energy levels. The selection rule for the dipolar transition between different energy levels is $\Delta m = \pm 1$, so a perturbation of angular frequency corresponding to the Larmor frequency is required.

This is illustrated in Fig. 2.1 for a nuclear spin $I = 3/2$, where three transitions take place, the transition from - $\frac{3}{2} \longleftrightarrow -\frac{1}{2}$ and $\frac{1}{2} \longleftrightarrow \frac{3}{2}$ are known as satellite transitions while the - $\frac{1}{2} \longleftrightarrow \frac{1}{2}$ represents the central transition [18].

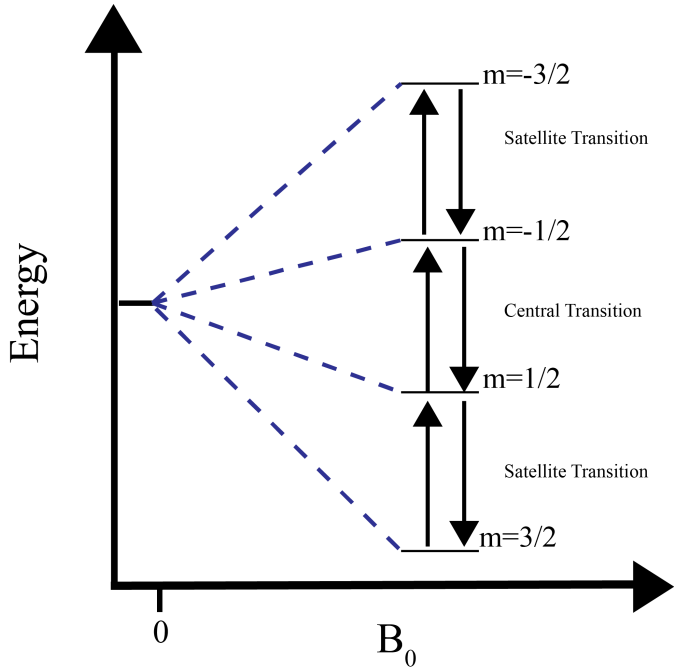

Figure 2.1: Energy levels of a $I = 3/2$ nuclear spin in an applied magnetic field B_0.

2.1.2 Macroscopic magnetization

The macroscopic magnetization M inside the material is defined as the sum of all the single magnetic moments μ_i of the nuclear spins.

$$M = \sum_i \mu_i \tag{2.7}$$

The longitudinal magnetization is the z-component of M (where $\hat{z}$ is the direction of the applied magnetic field), whereas the transverse magnetization is the component of M lying in the xy plane. Because nuclear spins precess around the magnetic field along the z-axis of the laboratory frame of reference, an individual nuclear moment has the same probability of being in any direction lying in the xy plane. The population of the energy levels at a certain temperature of equilibrium is governed by the Boltzmann distribution:

$$\frac{N_\beta}{N_\alpha} = e^{-\Delta E/(k_B T)}, \tag{2.8}$$

in which N_β and N_α are the number of particles in the states β and α, respectively, k_B is the Boltzmann constant, T is the temperature of equilibrium in the sample, and ΔE is the energy difference between the levels β and α [$\Delta E = E_\beta - E_\alpha = (+)\gamma\hbar\frac{1}{2}B_0 - (-)\gamma\hbar\frac{1}{2}B_0 = \hbar\gamma B_0$]. When ΔE is much smaller than kT then we obtain:

$$\frac{N_\beta}{N_\alpha} \approx 1 - \frac{\hbar\gamma B_0}{k_B T} \tag{2.9}$$

which is the high-temperature approximation. So that the population difference $\Delta N = N_\alpha - N_\beta$ and $N = N_\alpha + N_\beta$

$$\Delta N \approx N\frac{\hbar\gamma B_0}{2k_B T} \tag{2.10}$$

The equilibrium magnetization along the z-direction can be evaluated by multiplying the numbers of nuclei with the magnetic moment carried by each nucleus (along the z-axis):

$$M_{eq} = N\frac{\hbar^2\gamma^2 B_0}{4k_B T} \tag{2.11}$$

The transverse components of the magnetization average out to zero because of the destructive interference, since the individual spins are precessing all at the same angular frequency around the magnetic field, but their phases are completely random.

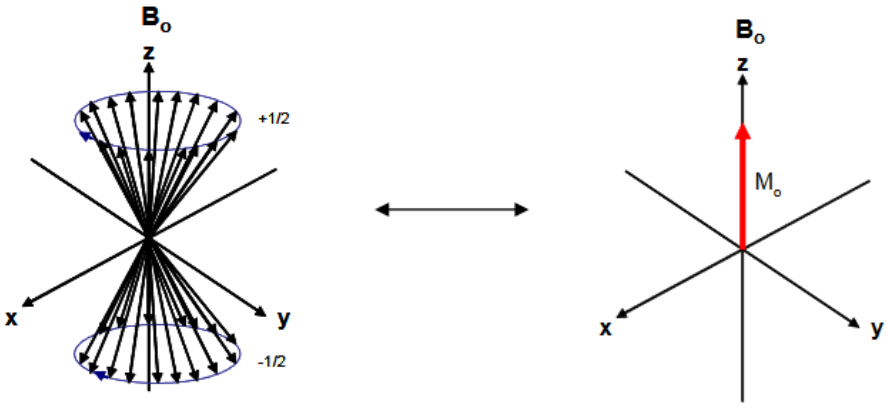

Figure 2.2: Transverse components of the magnetization and the equilibrium magnetization along the z-direction.

2.1.3 RF pulses and the rotating frame

The transverse components of the magnetization average is zero, as we see in Sec. 2.1.2, so that we apply radio frequency RF pulse to the sample for a short time to rotate the nuclear magnetization into the transverse plane with respect to the B field. The RF field generates an oscillating magnetic field,referred as B_1, which is produced by sending RF current into a coil wrapped around the sample, as shown in Fig. 2.3(a). Applying a magnetic field B_1 orthogonal to the external magnetic field B at the Larmor frequency ,let's say along the x-axis, will cause the magnetic moment

to precess in the (yz)-plane at frequency $\omega_1 = \gamma B_1$. If we apply B_1 for a time τ, the resulting magnetic moment will orient along the y-axis [19], such that:

$$\gamma B_1 \tau = \frac{\pi}{2} \tag{2.12}$$

is referred to as a $\pi/2$ or a 90° pulse, see Fig. 2.3(b).

If we apply B_1 for time twice $\pi/2$ pulse duration, the resulting magnetic moment will orient along the $-z$ direction, see Fig. 2.3(c).

$$\gamma B_1 \tau = \pi \tag{2.13}$$

is called a π or 180° pulse.

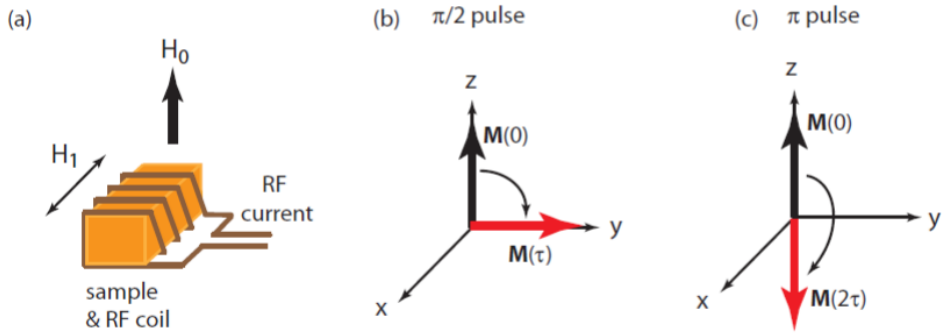

Figure 2.3: (a) The generation of oscillating magnetic field B_1 relative to the *RF* coil. (b) Schematic representation of a $\pi/2$ pulse (c) a $\pi/4$ pulse, generated by the application of the B_1 field [19].

2.2 Local interactions in the solid state

A local magnetic field is found at the nuclear site, where nuclear spins are interacting with their electronic environments, these interactions will shift and broaden the nuclear magnetic energy levels E_m and lead to relaxation effects.

Therefore, the NMR resonance condition Eq. 2.6 become:

$$\omega_{NMR} = \gamma(B + B_{loc}) \tag{2.14}$$

where B_{loc} is the local magnetic field, originates from the interaction of a nuclear spin with its magnetic environment like magnetic moments.

In general way, the Hamiltonian of the nuclear spin in a magnetic field expands to [20]:

$$\mathscr{H} = \mathscr{H}_Z + \mathscr{H}_{n-n} + \mathscr{H}_{n-e} + \mathscr{H}_Q \tag{2.15}$$

As depicted in Fig. 2.4, where $\mathscr{H}_Z$ is the Zeeman Hamiltonian has already been introduced in Eq. 2.4, $\mathscr{H}_{n-n}$ is the nuclear- nuclear interaction Hamiltonian, $\mathscr{H}_{n-e}$, is the nuclear-electron interaction Hamiltonian, the last contribution $\mathscr{H}_Q$ represents the electric quadrupole Hamiltonian. They will all be discussed in detail in the following.

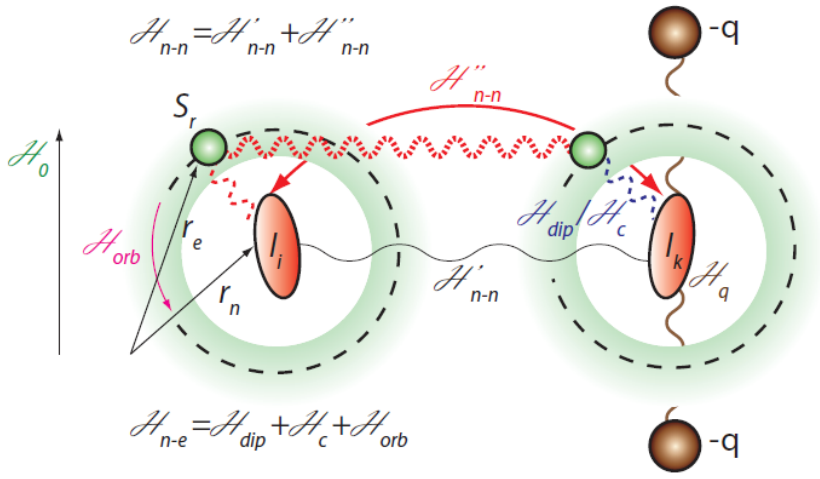

Figure 2.4: The representation of all terms involved in the general nuclear Hamiltonian [5].

2.2.1 Interactions between nuclear spins

The nucleus-nucleus interactions $\mathcal{H}_{n-n}$ between two nuclear spins $\vec{I}_i$ and $\vec{I}_j$ have been divided into the direct dipolar coupling and into indirect coupling:

$$\mathcal{H}_{n-n} = \sum_{i,j} \vec{I}_i a(\vec{r}_{ij}) \vec{I}_j = \mathcal{H}^{dir}_{n-n} + \mathcal{H}^{indir}_{n-n} \tag{2.16}$$

The nuclear magnetic dipoles are another sources of magnetic fields, which process in the applied magnetic fields at the Larmor frequency where the other nuclear dipoles see these dipolar fields which are usually of the order of a few Gauss [21]. So the direct dipolar Hamiltonian can be writen as:

$$\mathcal{H}^{dir}_{n-n} = \sum_{i<j}^{N} \frac{\gamma^2\hbar^2}{r^3_{ij}} \left[\vec{I}_i \cdot \vec{I}_j - 3\frac{(\vec{I}_i \cdot \vec{r}_{ij})(\vec{I}_j \cdot \vec{r}_{ij})}{r^2_{ij}} \right] \tag{2.17}$$

This is for general case of spins i and j. Where $\vec{r}_{ij}$ is the separation between thise two nuclear spins, the general direct dipolar coupling gives rise to a homogeneous broadening of the resonance line.

The second part of the coupling is the indirect coupling $\mathcal{H}^{indir}_{n-n}$ which is the electron-mediated interactions, can be expressed as:

$$\mathcal{H}^{indir}_{n-n} = \vec{I}_i a_{ij} \vec{I}_j \tag{2.18}$$

where the coupling tensor a_{ij} depends on the coupling mechanism. The hyperfine interactions between nuclear spin and a surrounding electron is one way of the indirect coupling between the two nuclear spins as we will see in the following section

2.2.2 Hyperfine interaction

The nuclear-electron interaction or hyperfine interaction is the magnetic interaction of electronic states such as electronic spin $\vec{S}$ and the orbital momentum $\vec{L}$ of the

electrons with a nucleus spin $\vec{I}$, the hyperfine Hamiltonian $\mathscr{H}_{hf}$ in general form can be written as.

$$\mathscr{H}_{hf} = \gamma_{\mathrm{n}}\gamma_{\mathrm{e}}\hbar^2\vec{I}\cdot\left[\left(3\frac{(\vec{S}\cdot\vec{r})\cdot\vec{r}}{r^5}-\frac{\vec{S}}{r^3}\right)+\frac{8\pi}{3}\vec{S}\delta\vec{r}+\frac{\vec{L}}{r^3}\right] \tag{2.19}$$

where r is the separation between electron and nucleus.

Dipolar coupling: The first term $\mathscr{H}_{dip}$ describes the dipolar interaction between nucleus magnetic moment and electron magnetic momentum, which is made if the distance between these two spins is large enough, where is the case for p- , d- and f -orbitals, not for s-electrons. The dipolar interaction leads to dipolar shift K_{dip}, this term is anistropic.

Contact interaction: The second term $\mathscr{H}_c$ describes the Fermi contact interaction arises from the direct coupling between the nuclear spin and the spin of unpaired s-electrons leading to contact shift K_{contact}. In the same way as the Fermi contact contribution there is a core polarization which describes the polarization of the spins from unfilled outer electronic shells, even closed s-shells leading to core shift K_{core}. where these two terms are isotropic.

Orbital contribution: The last term $\mathscr{H}_{orb}$ in Eq. 2.19 is the so called orbital interaction. It is due to the effective field created by electrons which possess a non zero orbital angular momentum $\hat{L}$ of the electron and the nuclear spin $\hat{I}$ leading to orbital shift K_{orb}.

Knight shift

In paramagnetic metals there are displacements of the NMR frequency with respect to the frequency of the free nuclei, the resonance field shift which is determined by the local spin polarazation of the conduction electrons known as Knight shifts with the abbreviation K, or hyperfine coupling between nuclear spin and conduction electrons.Together with the Zeeman term, one obtains :

$$\mathscr{H}_Z + \mathscr{H}_{n-e} = -\gamma\hbar\vec{I}(1+\mathbf{K})\vec{H}_0 \tag{2.20}$$

where **K** is the Knight shift tensor. The observed resonance frequency will express the expected Larmor frequency ω_{L} shifted by the Knight shift K_{z} for a measurement along the z- axis:

$$\omega_{\mathrm{obs}} = (1+K_{\mathrm{z}})\omega_{\mathrm{L}} \tag{2.21}$$

The Knight shift covering all different couplings between nuclear spins and electronic spins.

$$K = K_{\mathrm{dia}} + K_{\mathrm{orb}} + K_{\mathrm{s}} \tag{2.22}$$

where K_{s} is the spin shift ($K_{\mathrm{s}} = K_{\mathrm{dip}} + K_{\mathrm{contact}} + K_{\mathrm{core}}$) and K_{dia} is the diamagnetic shift arises from the diamagnetism of the ion cores and the Landau diamagnetism of the conduction electrons, diamagnetic shifts are very small so they can be neglected.

2.2.3 The quadrupole interaction

The charge distribution is perfectly symmetric when the spin I of the nuclei is $1/2$ where nuclei behave like point charges. In contrast to nuclei with $I > 1/2$ the charge distribution will be ellipsoidal having an nuclear quadrupole moment Q [17]. The surrounding electric charge distribution produce an electric field gradient interact with the nuclear quadrupole moment described by the quadrupole Hamiltonian $\mathscr{H}_Q$.The electric field gradient is a second rang tensor defined as:

$$V_{ij} = \frac{\partial^2 V}{\partial x_i x_j} \quad \text{with} \quad i,j = x,y,z \tag{2.23}$$

where V is the electrostatic potential. The quadrupole Hamiltonian $\mathscr{H}_Q$ can be expressed as:

$$\mathscr{H}_Q = \frac{e^2 qQ}{4I(2I-1)}[3I_z^2 - I^2 + \eta(I_x^2 - I_y^2)] \tag{2.24}$$

where e is the charge of the electron, q is the electronic quadrupole moment, V_{XX}, V_{yy} and V_{ZZ} are the diagonal elements of the electric field gradient tensor which is traceless ($\nabla^2 V = 0$):

$$V_{xx} + V_{yy} + V_{zz} = 0 \tag{2.25}$$

It is common to use $V_{zz} \geq V_{xx} \geq V_{yy}$ and $eq \equiv V_{zz}$. For spherically-symmetrical charge distribution the quadrupole interaction vanishes where in this case $V_{xx} = V_{yy} = V_{zz} = 0$. then we can also use the asymmetry parameter:

$$\eta = \frac{|V_{xx} - V_{yy}|}{V_{zz}} \tag{2.26}$$

The effect of the quadrupole interaction in strong magnetic field, where $\nu_L \gg \nu_q$, $\nu_L = \omega_L/2\pi$, is to split the principle resonance line in to $2I$ resonance lines and the quadrupole Hamiltonian $\mathscr{H}_Q$ will be the perturbation of the Zeeman Hamiltonian $\mathscr{H}_Z$. The change of energy in first order expansion can be expressed as:

$$E_m^{(1)}(\theta,\varphi,\eta) = \frac{1}{4} h \nu_q (3\cos^2\theta - 1 + \eta \sin^2\theta \cos 2\varphi)\left[m^2 - \frac{1}{3}I(I+1)\right] \tag{2.27}$$

In the first-order quadrupole correction the frequencies from the central peak ($m \longleftrightarrow m+1$) can be expressed as :

$$\omega_{m,m+1} = \omega_Q (m - 1/2)(3\cos^2\theta - 1 + \eta \sin^2\theta \cos 2\varphi) \tag{2.28}$$

where θ and φ are the angels between the applied field direction and the principle axes of the electric field gradient (X, Y, Z). The quadripolar frequency (ν_q) equal

$$\nu_Q = \frac{3eQV_{ZZ}}{2I(2I-1)h} = \frac{3e^2qQ}{2I(2I-1)h} = \omega_Q/2\pi \tag{2.29}$$

The central transition is unaffected to first order in the quadrupole perturbation, but is shifted by $(e^2qQ)^2/\gamma\hbar$ by second order perturbation. If we take for example

$I = 3/2$ in an uniaxial symmetry ($\eta = 0$) and in a strong applied magnetic field, the level splitting for $\theta = 0°$ and $\theta = \pi/2$ shown in Fig. 2.5.

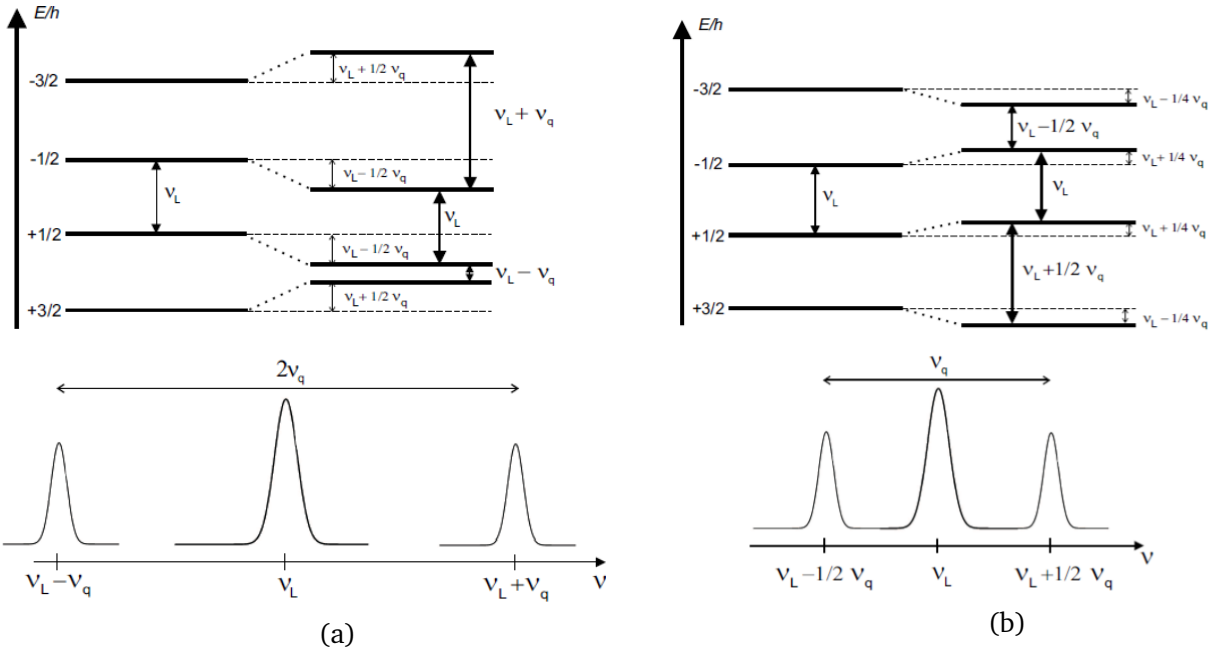

Figure 2.5: Level splitting for $I = 3/2$ in an uniaxial symmetry ($\eta = 0$) in a strong magnetic field with two different orientations of the electric field gradient in the field (a) for $\theta = 0°$ (b) for $\theta = \pi/2$.[20]

Fig. 2.6 displays the effects of all the possible interactions on the energy levels and, hence, the related transition frequencies, in the case $I = 3/2$, $\eta = 0$, $\theta = 0°$, and $V_{zz} \neq 0$. These considerations are valid under the assumption of a Zeeman perturbative regime, i.e., $\mathcal{H}_Z \gg \mathcal{H}_Q$

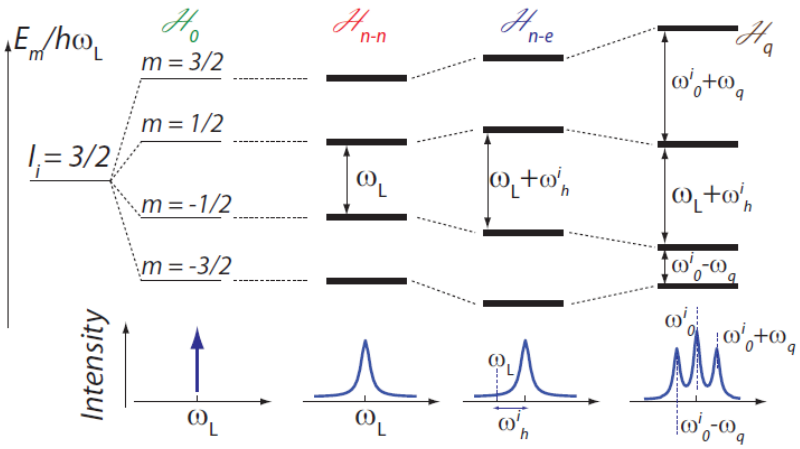

Figure 2.6: Summary of all possible interactions, $\mathcal{H}_Z$,$\mathcal{H}_{n-n}$,$\mathcal{H}_{n-e}$ and $\mathcal{H}_Q$ for $I = 3/2$ [5].

All formulas in this section,which describe the nuclear quadrupole moment interaction with electric field gradient, are valid for single crystals where the angles θ and

φ between the applied field B and the crystalline frame, have well-defined values. In a powder made crystallite (i.e., $Ce_xLa_{1-x}NiGa_2$ series) oriented randomly with respect to B [21, 22]. Its shape can be calculated by second-order quadrupole correction, where the resonance frequency of the central transition will shift by second-order quadrupole shift [23]:

$$\omega_{-\frac{1}{2},\frac{1}{2}} = -\frac{\omega_Q^2}{6\omega_L}\left[I(I+1)-\frac{3}{4}\right][A(\varphi,\eta)\cos^4\theta + B(\varphi,\eta)\cos^2\theta + C(\varphi,\eta)] \quad (2.30)$$

where A, B, and C depend on angle φ and asymmetry parameter η (their expressions can be found in Ref. [22]). Fig. 2.7 display the first-order splitting of satellites and second-order broadening and shifting of central component , for powder pattern for a nucleus of spin $I = 3/2$ [24].

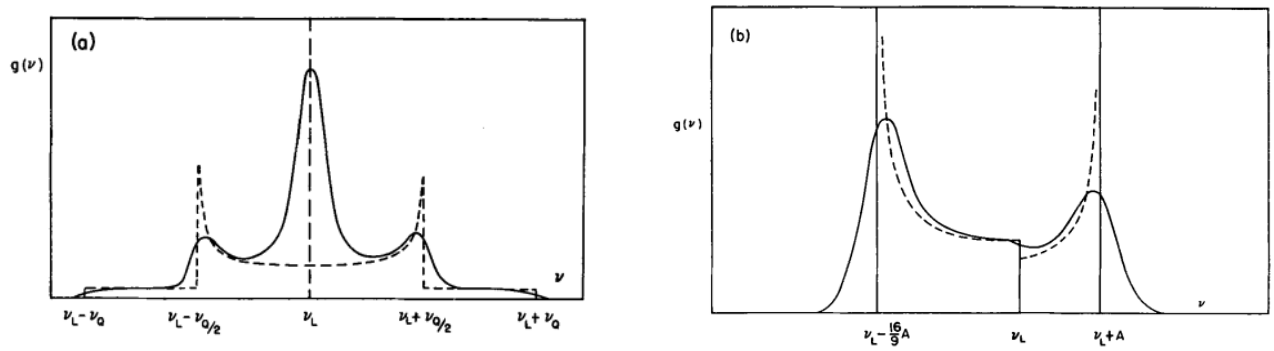

(a) (b)

Figure 2.7: Quadrupole splitting of the magnetic resonance for a powder patterns for $I = 3/2$ (a) First-order pattern (b) second-order pattern.[24]

2.3 Relaxation phenomena

After the B_1 field is turned off, the nuclear spins will evolve to return back to their original thermal equilibrium which is called NMR relaxation. This process occurs in a finite time, depending on the magnetic environment of the nuclear spins and the thermodynamic condition of the sample. At a practical level, the rate of relaxation determines how fast an experiment can be repeated, so it is important to understand how relaxation rates can be measured and the factors that influence their values. The rate of relaxation is influenced by the physical properties of the molecule and the sample, so a study of relaxation phenomena can lead to information on these properties. Bloch has introduced equations considering the nuclear spin dynamics and relaxation processes describing the precession of M around B, known as the Bloch equations:

$$\frac{dM_x}{dt} = \gamma(M \times B)_x - \frac{M_x}{T_2} \quad (2.31)$$

$$\frac{dM_y}{dt} = \gamma(M \times B)_y - \frac{M_y}{T_2} \quad (2.32)$$

$$\frac{d\,M_z}{d\,t} = \gamma(M \times B)_z - \frac{M_0 - M_z}{T_1} \tag{2.33}$$

The relaxation is characterized by T_1 and T_2, which are called spin-lattice relaxation time and spin-spin relaxation time, respectively, (relaxation rates $R_1 = 1/T_1$ and $R_2 = 1/T_2$ are also used) These two quantities are two time constants both occur at the same time, characteristic of the system as explained in the following. Figure 2.8 shows an example for each of these mechanisms.

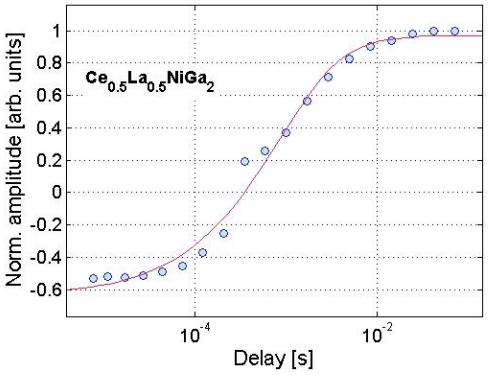

(a)

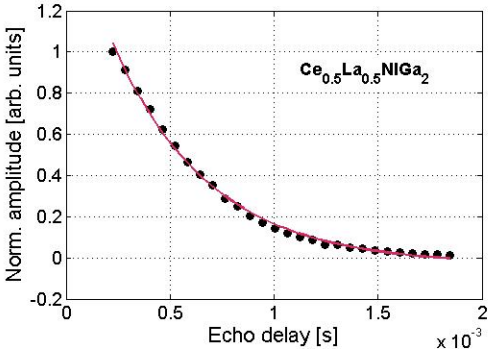

(b)

Figure 2.8: Plots reporting the results of two different relaxation-time measurements in $Ce_{0.5}La_{0.5}NiGa_2$: (a) T_1 measured at 20 K, and (b) T_2 measured at 20 K.

2.3.1 Spin-lattice relaxation time T_1

The longitudinal component of the nuclear magnetization return back to its equilibrium position in a characteristic time T1, when moved away from it, giving it the name of longitudinal relaxation. This relaxation is a consequence of the energy minimization, which is caused by an exchange of energy between the nuclear spins and its environment, such as the surrounding electronic lattice spins, giving it the name of spin-lattice relaxation. These lattice spins affects the nuclear spins by generating local magnetic fields, in particular transverse ones. The transverse fields oscillating on resonance are the most effective in relaxing the macroscopic magnetization. Their effect on the individual spins is to induce a transition from one spin state to another when the energy difference between those states is exactly $\Delta E = \hbar\omega$. Since states with the spin aligned along the field direction are at a lower energy state, transition to these states will be favored in terms of probability, thus allowing the magnetization to be restored to its original equilibrium value By solving the equation Eq. 2.33 we get for a 90° (B_1) RF pulse:

$$M_z(t) = M_0(1 - e^{-t/T_1}) \tag{2.34}$$

For a 180° inversion (B_1) RF pulse,

$$M_z(t) = M_0(1 - 2e^{-t/T_1}) \tag{2.35}$$

The process of T_1 relaxation after a saturation pulse(90° rf pulse) is applied at equilibrium where M_z is reduced to zero, but then recovers back to its equilibrium value

along the z-axis if no further rf pulses are applied as we will describe that in more detail later on.

T_1 can be calculated by using the following equation:

$$\ln(I_0 - I) = \ln 2I_0 - \frac{t}{T_1} \tag{2.36}$$

where I is the initial intensity of the signal at t= τ, and I_0 is the limiting value of I for a very long interval (t = ∞). When $M_z = 0$ thus t $\equiv \tau_{null} = T_1 \ln 2$. Therefore, T_1 for all peaks in the spectrum equals:

$$T_1 = \frac{\tau_{null}}{\ln 2} = 1.443\tau_{null} \tag{2.37}$$

In general, the nuclear magnetization recovery for $I \geq 1$ is a multiexponential function given by [8]:

$$\frac{m_\infty - m(t)}{m_\infty} = \sum_i a_i exp(\frac{-b_i t}{T_1}) \tag{2.38}$$

when $\mathscr{H}_Z \gg \mathscr{H}_Q$, assuming magnetic relaxation only, the coefficients (a_i and b_i) for the magnetization recovery function are ($b_1 = 1, b_2 = 3, b_3 = 6$) and $a_i's$ for central transition (- $\frac{1}{2} \leftrightarrow \frac{1}{2}$) are ($a_1 = 0.1, a_2 = 0, a_3 = 0.9$) :

$$1 - \frac{m(t)}{m_\infty} = 0.1e^{-(t/T_1)} + 0.9e^{-6(t/T_1)} \tag{2.39}$$

and for satellite transitions ($\pm\frac{1}{2} \leftrightarrow \pm\frac{3}{2}$) $a_i's$ are ($a_1 = 0.1, a_2 = 0.5, a_3 = 0.4$)

$$1 - \frac{m(t)}{m_\infty} = 0.1e^{-(t/T_1)} + 0.5e^{-3(t/T_1)} + 0.4e^{-6(t/T_1)} \tag{2.40}$$

Korringa Relation

In isotropic materials only the contact-term survives, since all other terms average out to zero. Under this approximation, the *Korringa relation* can be derived:

$$K^2 T_1 T = \frac{\hbar}{4\pi k_B} \frac{\gamma_e^2}{\gamma_N^2} = S_0 = const. \tag{2.41}$$

where γ_e is the electron gyromagnetic ratio (2.8024×10^4 MHz/T), γ_N is the nuclear gyromagnetic ratio (i.e., ^{71}Ga equal 13.0207 MHz/T) and k_B is the Boltzmann constant. The Korringa ratio can be defined as $\alpha = S_0/(K^2 T_1 T)$ which is determined by a different sources, such as electron-electron interactions, and exchange enhancement[25]. Measuring α allows for a consistency check of the model:

- $\alpha = 1$, reflects the behavior of a Fermi gas (normal metal without any correlations).
- $\alpha < 1$, The observed system has tendency towards antiferromagnetic correlations at $\vec{q} \neq 0$.

- $\alpha > 1$, The observed system has tendency towards ferromagnetic correlations at $\vec{q} = 0$.

However, we have to be careful when doing a quantitative interpretation based on the value of α. Where it was shown that disorder may enhance α [25]. For paramagnetic isotropic metals:

$$\frac{1}{T_1 T} \equiv \text{constant} \tag{2.42}$$

When dealing with non-isotropic or nonmetallic materials, deviations from this law are expected.

2.3.2 Spin-spin relaxation time T_2

This phenomenon is associated with the spontaneous entropy increase and is responsible for the decay of the transverse component of the magnetization. It is caused by the presence of longitudinal local fields, that produce slight variations in the magnitude of the longitudinal component of the magnetic field experienced by each individual nucleus. These cause the individual nuclei to precess at slightly different rates, causing the macroscopic transverse magnetization to vanish after a determined lapse of time. These longitudinal local fields arise mainly from other spins of the same nuclear species, so that this relaxation process is called also spin-spin relaxation. The characteristic time constant associated with this decay process is conventionally named T_2. In contrast to the longitudinal case, the transverse relaxation conserves the (magnetic) energy. We also note that inhomogeneities in the externally applied magnetic field contribute to the decay of the transverse magnetization. However, as we will show in Sec. 3.2.3, the magnetization loss caused by field inhomogeneities can be recovered by means of a spin-echo sequence since, in contrast to the local fields, these are constant in time.

To determine T_2 we solved Eq. 2.32 for M_y :

$$\begin{aligned} M_y &= M_0 e^{-t/T_2} \\ \ln M_y &= \ln M_0 - t/T_2 \end{aligned} \tag{2.43}$$

T_2 is determined from the slope of $\ln I$ vs t,

$$\ln I = \ln I_0 - \frac{t}{T_2} \tag{2.44}$$

Chapter 3

NMR: experimental aspects

3.1 Experimental methods

3.1.1 Detection of the NMR signal

Nuclear magnetic resonance (NMR) signals detected by the precession of the total magnetization arising from the electrons, where the total magnetization arising from the nuclei is negligible. The pulsed- NMR experiment is obtained by the application RF pulse to our sample by placing it inside a RF coil, in the axis of the coil perpendicular to the applied magnetic field (in the xy-plane) where the fundamental idea of it is rotating the magnetization onto the transverse plane to detect an AC current, as has already been explained in Sec. 2.1.3. For the RF pulse we use RLC circuit to maximize the pick-up AC current as well as to maximize the power transmit to the nuclear spin system, both being restricted by the mean frequency and the bandwidth of the circuit resonance.Thus, two variable capacitors are responsible for variation of the frequency and the width of the coil resonance, depending of the frequency of the RF pulse used.

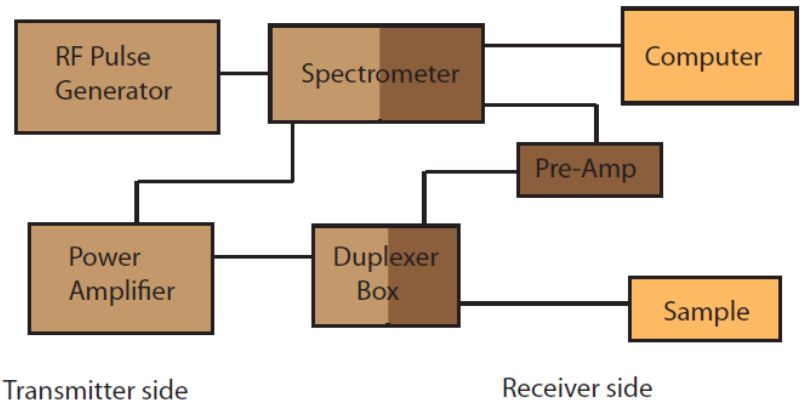

Figure 3.1: Simplified block digram of the main components of a typical NMR experiment. [19]

In the transmitter side of the experiment the low power RF generator feeds the

spectrometer which switch on and off the wave into a square pulse. By external power amplifier the pulse is amplified and transmitted to the RF coil. On the receiver side, by using an amplifier the weak detected AC current is amplified and returned back to the spectrometer and after that the AC current is processed and displayed by a computer. A duplexer box prevents the powerful pulse from going back to the spectrometer, but allows the weak signal to do so. [19]

3.1.2 The probe circuit

The most interesting part of the NMR spectrometer is the probe which has a small coil held at the top of the probe, used for both the signal detection and for the transmission of the transverse RF pulse. The coil is normally hand- made, by wrapping a copper wire of 0.3 mm diameter around a cylindrical object with approximately the same diameter of jelly capsules where the sample inserted in[26].

The coil forms part of a resonant LC-circuit, as shown in Fig. 3.2, there are two capacitors in LC-circuit also one in parallel with the coil where when changing it will cause the resonance frequency of the circuit to move (tunning) and the second one is in series with the coil, when changing in it will affect the impedance value of the circuit (matching). To maximize pulse power absorption and promote signal detection we have to tune the circuit at the sample's resonant frequency (i.e., $\gamma =$ 65.003 MHz for ^{71}Ga at I=3/2 and 5 T). For frequencies in the radio range, i.e., 10 $-$ 150 MHz, capacitors of $\sim$ 100 pF are used in combination with handmade coils of $\sim$ 0.1 H.

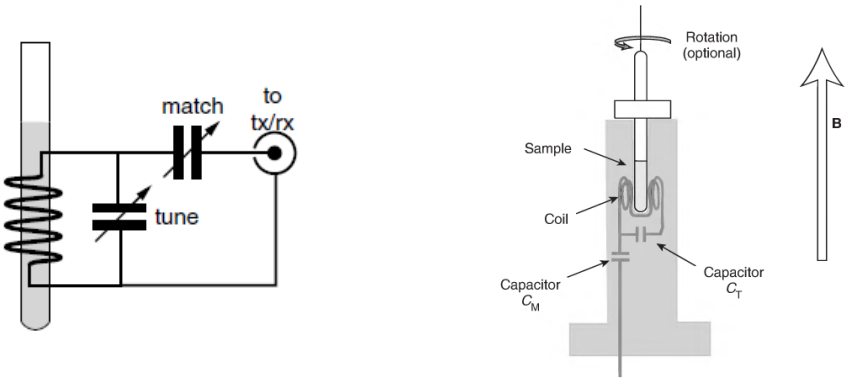

(a) (b)

Figure 3.2: (a),(b) Schematic of a simple single-frequency probe circuit [26].

3.1.3 Free induction decay

The simplest pulse NMR experiment start by launching one RF pulse to a sample placed in a uniform magnetic field B in z-direction, to rotate the nuclear spin magnetization into the xy plane, this transverse magnetization is detected by NMR experiment, unlike longitudinal magnetization. After $\pi/2$ pulse with matching frequency, power and duration, where the pulse duration is a period time of switching on the oscillating magnetic field B_1 (pulses), a voltage is detected on the receiver

coil via Faraday induction referred as the free induction decay FID. At the resonance frequency the signal will decay exponentially which is characterized by the spin-spin relaxation time constant T_2 of the sample, as shown in Fig. 3.3. It contains information on the environment of the spin.

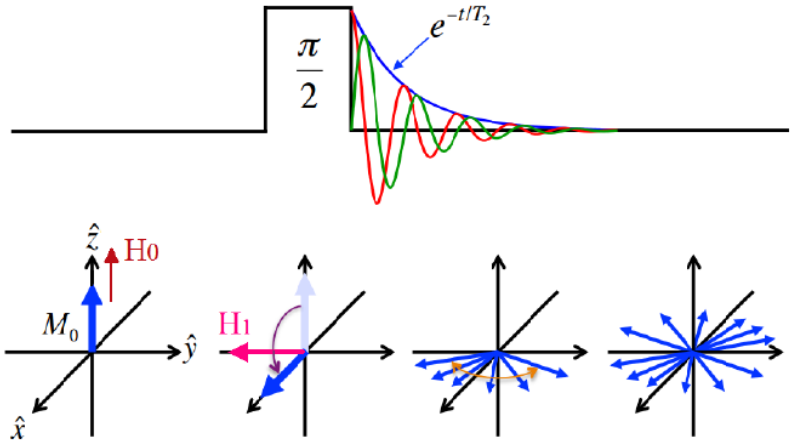

Figure 3.3: The free induction decay measuring after one single RF pulse. [27]

3.1.4 The spin-echo sequence

The spin echo (Hahn echo) was developed by Erwin Hahn in 1950, to resolve the problem of fast decaying FID's, where it is difficult to observe the initial part of the FID due to the dead time which is the finite recovery time of the receiver. The spin echo sequence is used to eliminate the dephasing of the precessing magnetic moment. In the following, we describe a $\pi/2-\tau-\pi-\tau$ acquire pulse sequence proposed by Carr-Purcell method, as shown in Fig.(3.4). The first $\pi/2$ pulse(frequency f, duration D1, amplitude A) produces a rotating nuclear magnetization on the xy plane which the coherence of its magnetic moments loses with time τ as in the FID. A π pulse (frequency f, duration D2, amplitude A) is applied after a spacing time τ, which produce an inversion of the spins. All the spins will refocus at time τ after the π pulse form the spin echo.

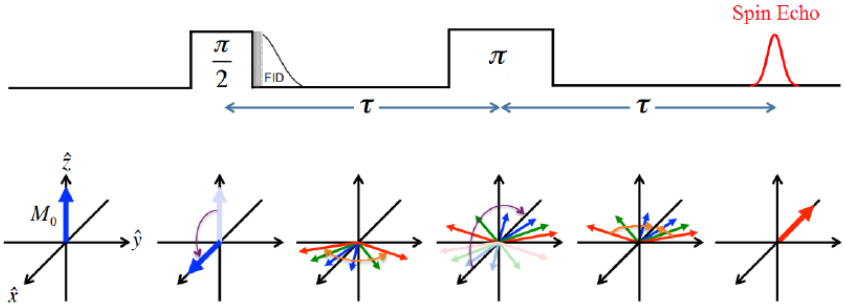

Figure 3.4: Spin-echo pulse sequence, where show the time evolution of nuclear magnetism and also demonstration of the applied pulses and the detected signals.

3.2 Experimental procedures

3.2.1 Line-shape measurements

The line-shape measurement or line acquisition consists in acquiring a signal by averaging over multiple scans, and when a satisfactory signal-to-noise ratio has been reached, the measurement can be interrupted and the data are digitally saved in a computer memory. The last are then imported in a software for numerical calculations, which allows to carry out a discrete Fourier transformation. The so obtained values represent the NMR line and can be subsequently saved and plotted.

It is important, for this kind of measurements, to set a long enough relaxation delay between successive scans. This delay allows the magnetization to reach its equilibrium value after the spin-echo pulse sequence, thus increasing the signal intensity of the subsequent scan. This increases the signal-to-noise ratio and allows to reduce the number of necessary scans.

The RF pulse has a specific frequency band associated with its finite length. In some cases, however, the natural width of the NMR line may be larger than the pulse bandwidth. In these cases, it is necessary to perform a frequency-sweep experiment, in which line acquisitions centered at different frequencies are performed successively, so as to cover the whole frequency range. The different acquisitions are then summed up, in order to obtain the complete NMR line.

3.2.2 Spin- lattice relaxation rate measurement

In our experiments the technique that are used to measure the spin-lattice relaxation time T_1 with spin echoes is the inversion recovery method, as pictured in Fig. 3.5(a), consists in applying a π pulse to the sample in order to invert the magnetization to the$-z$ axis. After delay time τ, one performs a spin-echo sequence and measures the intensity of the acquired line, which is proportional to the magnetization value. The data are then fitted according to an exponential law of the central transition recovery curve for the magnetic contribution for $I = 3/2$ as Eq 2.39.

There is, however, another method that allows to measure T_1 in a shorter time with respect to the time needed by using inversion recovery. This is called saturation recovery and consists of two sets of pulses: the initial pulse is the saturation pulse which is a $\pi/2$ pulse, this pulse knocks the spins down on the xy plane. By waiting for a certain delay time τ, some of the longitudinal magnetization M_z will have started to partially relax back to its equilibrium value. The strength of the signal that will be detected by spin echo sequence proportion to this partial magnetization. For a particular delay time, the magnitude of the NMR signal is detected by a $\pi/2 - \pi$ spin-echo pulse sequence. In Fig 3.5(b) show the spin-echo intensity versus delay time where the constant of the exponential growth is T_1 as explained in Eq. 2.41.

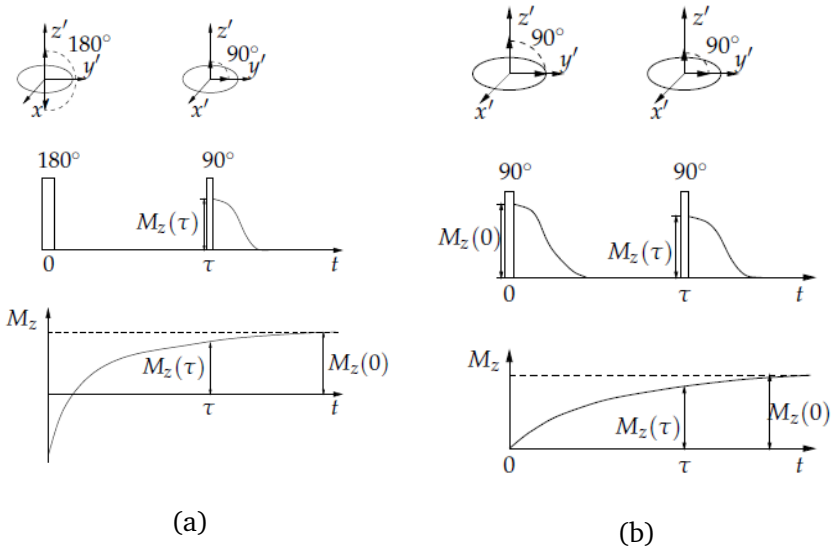

Figure 3.5: (a) Inversion recovery pulse sequence. (b) Saturation recovery pulse sequence. [28]

3.2.3 Spin- spin relaxation rate measurement

The spin echo technique is an efficient and easy way to measure the spin-spin relaxation time T_2, as shown in Fig. 3.6. Thus, T2 is acquired by applying a succession of $\pi/2-\tau-\pi-\tau$ acquire spin echo pulse sequence using a range of values of the delay time τ. After the $\pi/2$ knocks the magnetization down on the xy plane, the transverse magnetization start fanning out and lose their coherence as the delay time increases and after that the π pulse flips the spins where they refocus giving a spin echo signal. The transverse magnetization decays will increase as the delay time increases. The data are then fitted according to Eq. 2.43.

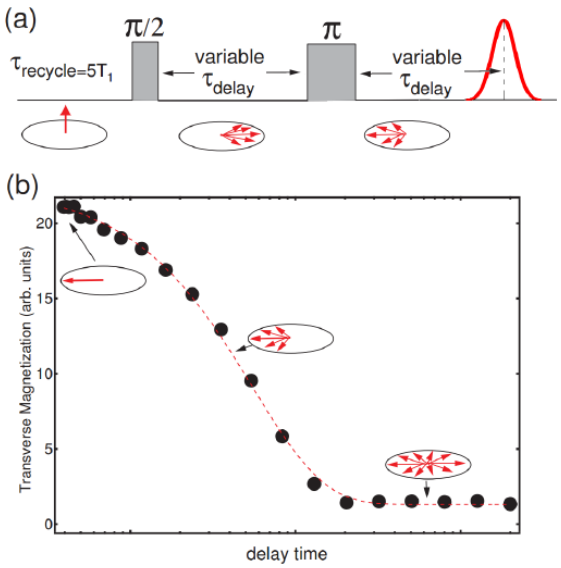

Figure 3.6: Measurement of spin-spin relaxation time T_2 by echo decay sequence.

3.3 Experimental techniques

We report on Ga nuclear magnetic resonance NMR measurements on the new heavy-electron compounds $Ce_xLa_{1-x}NiGa_2$ series over a wide temperature range, from 100 mK up to 300 K. where all attention have focused on the ^{71}Ga nucleus in all samples which has nuclear spin $I = 3/2$ with Larmor frequency in our applied magnetic field (5.0072 T) equals 65.003 MHz. We have received all the samples in form of powder.

The NMR measurements included line-shape, spin-lattics relaxation time T_1 and spin-spin relaxation time T_2 data. The experiments on these powders were performed sealing the sample in Teflon (PTFE) tubes fixed inside the RF coil. The NMR signals were monitored by means of standard spin-echo sequences, consisting in $\pi/2$ and π pulses. For our samples, we have chosen a $\pi/2$ pulse of 3 to 4 μs duration time, with the recycle delays ranging from 2 s to 50 ms, depending on the temperature ranging from between 0.1 and 300 K. The spin-lattice relaxation times T_1 were measured with the inversion recovery method, that were discussed in sec. 3.2.2, using a $\pi - \pi/2 - \pi$ pulse sequence. The ^{71}Ga NMR spectra were obtained via the fast Fourier transformation (FFT) of the echo signal.

3.4 Samples: the $RENiGa_2$ compounds

3.4.1 Structure

$RENiGa_2$ compounds, where RE is one of the rare-earth elements La and Ce, crystallize in an orthorombic system (space group C m m m). The RE element is located in a single inequivalent site, while Ga atoms can occupy three different inequivalent sites Ga1, Ga2, and Ga3, with coordinates (0.5 0 0), (0 0 0.5), and (0 y 0.5), respectively. This implies that the crystal electric-field splits the energy levels of the Ce^{3+} $4f$-electrons Hund's rule ground state ($J = 5/2$) into three doublets. $LaNiGa_2$ and $CeNiGa_2$ have similar lattice parameter a,b,c, measured in $A°$: (4.29 17.83 4.27) and (4.22 17.59 4.18), respectively. In both $LaNiGa_2$ and $CeNiGa_2$ the RE exists in the form of a RE^{3+} cation, meanning that the electronic configuration of La^{3+} is simply [Xe] and of Ce^{3+} is [Xe] $4f^1$.

In order to identify the influence of $4f$-electrons, NMR measurements were also made by using $LaNiGa_2$ as sample of reference compound and $CeNiGa_2$ as sample under study, as done already on $REPd_2In$, always with RE=La,Ce [29].

3.4.2 Thermodynamic and transport properties

Transport, specific heat and magnetic susceptibility measurements on $CeNiGa_2$ and $LaNiGa_2$ compounds have been already comparatively studied in 1995 [30]. It emerged that $LaNiGa_2$ is a centrosymmetric intermetallic and superconductor with T_c = 2 K, while $CeNiGa_2$ is a heavy-fermion metal exhibiting a maximum Kondo effect at $T_K = 33.9$ K undergoing an antiferromagnetic (AFM) transition at about T_N= 3.5 K. Above T_K, the temperature dependence of the magnetic susceptibility, $\chi(T)$, follows a Curie-Weiss law with a paramagnetic Curie temperature of θ_P = -60 K and an effective

moment $\mu_{\text{eff}} = 2.64\ \mu_{\text{B}}$ [30]. Anomalies in the temperature dependence of $\chi(T)$, of the specific heat $C_{\text{P}}(T)$ and the electrical resistivity $\rho(T)$ indicate a phase transition to an antiferramagnetic phase at $T = 4\,\text{K}$.

Chapter 4

Results and discussion

4.1 NMR measurements on the $RENiGa_2$ compounds

4.1.1 NMR spectra of $Ce_{0.5}La_{0.5}NiGa_2$

In Fig. 4.1 we show one example of the ^{71}Ga NMR spectrum of $Ce_{0.5}La_{0.5}NiGa_2$ at applied magnetic field of 5.0072 T and a temperature of 50 K. The prominent peak in this figure correspond to the central line $1/2 \leftrightarrow$ -1/2 for the isotop ^{71}Ga . The sharp lines correspond to NMR resonances of ^{65}Cu and ^{63}Cu from the NMR coil, the vertical broken line mark the position of the Larmor frequency for ^{71}Ga, as indicated in the figure.

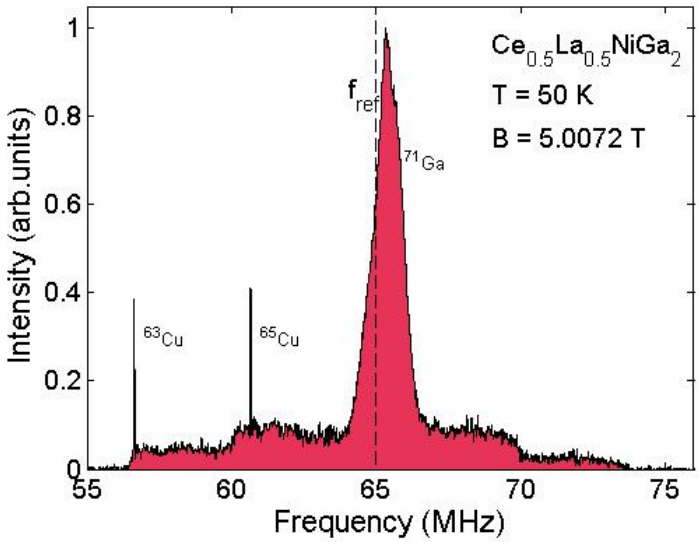

Figure 4.1: NMR-spectrum of $Ce_{0.5}La_{0.5}NiGa_2$ at a temperature of 50 K and a field 5.0072 T K for a randomly oriented powder, the sharp lines correspond to NMR resonances of ^{65}Cu and ^{63}Cu from the NMR coil, the vertical broken line mark the position of the Larmor frequency for ^{71}Ga.

4.1.2 Line-shape evolution

Figures 4.2 display the evolution with cerium content x of the height-normalized ^{71}Ga NMR line shapes in $Ce_xLa_{1-x}NiGa_2$ at two different temperature 10 K ($< T_K$) and 50 K ($> T_K$) in magnetic field (5.0072 T). The position of the observed peaks are shifted and NMR lines broaden upon increasing the substitutional La-for-Ce level atom in the samples for both temperatures. Figures 4.3 and 4.4 resume the outcome of the analysis performed on the line-shapes: the frequency shifts plotted vs. the substitutional La-for-Ce level in the sample (Fig. 4.3) and the line-width plotted vs. the substitutional La-for-Ce level in the sample (Fig. 4.4). The shifts were measured by considering the line maxima, while the widths were measured at half height of the normalized lines.

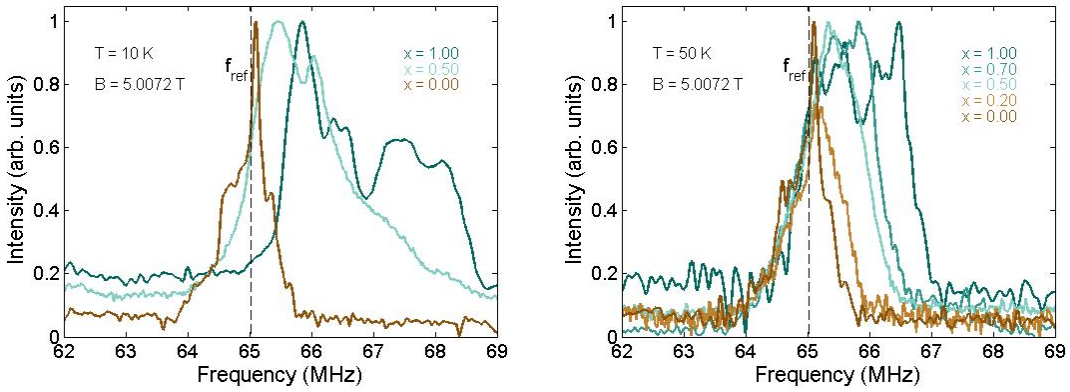

(a) (b)

Figure 4.2: ^{71}Ga NMR line shapes in $Ce_xLa_{1-x}NiGa_2$ measured at 10 K (a) and 50 K (b), for different values of cerium content x. The vertical broken line mark the position of the Larmor frequency for ^{71}Ga.

From a first sight at Fig. 4.2, one already realizes that the our samples reproduce many of the features that were discussed in Chap. 2: strong temperature dependent frequency shifts and broadening of the lines at low temperatures below Kondo temperature. Moreover, strong substitutional La-for-Ce level dependent frequency shifts and broadening of the lines.

The Knight shift due to the Pauli paramagnetism of the conduction electrons can be expresses as:

$$K_0 = \frac{\gamma_0 + \gamma_{\text{ref}}}{\gamma_{\text{ref}}} \tag{4.1}$$

where γ_{ref} is the Larmor frequency of the ^{71}Ga nucleus in the applied magnetic field (65.003 MHz) and γ_0 is the frequency of the peak maxima. In the absence of f-electrons, when the percent of the Ce equal zero, the Knight shift will express as Eq. 4.1, where the value of the shift for $LaNiGa_2$ at 10 K and 50 K are close as seen in Fig. 4.2. In intermetallic compounds having cations (such as Ce^{3+}) with shell incompletely filled of f-electrons, will have an interaction between the conduction electrons with these f-electrons which affect on the NMR line shift that measured at

the nuclei of non magnetic ligand ions resulting in

$$K = K_0\left(1 + \frac{g_J}{4J_{sf}C}\right) = K_0 + \frac{H_{hf}}{N_A\mu_B}\chi \tag{4.2}$$

with

$$C = \frac{2J_{sf}^2(g_J - 1)\chi_f}{N_A\mu_B^2 g_J^2} \tag{4.3}$$

where g_J is Landé g-factor for the Ce^{3+} cation $= 6/7$, J_{sf} is the s-f exchange interaction constant , N_A is Avogadro's number and χ_f is the f-electron susceptibility $\chi_f = \chi_{CeNiGa_2} - \chi_{LaNiGa_2} \approx \chi_{CeNiGa_2}$ is obtained from measurments of the magnetic susceptibilities of both compounds [30].

In Fig. 4.3 we confirm the linear relation between the Knight shift and the substitutional La-for-Ce level of the samples. The solid line represents a linear fit of the data. The shift values changing smoothly from about 0 to 2.7 MHz for $T = 10$ K and from 0 to 0.7 MHz for $T = 50$ K.

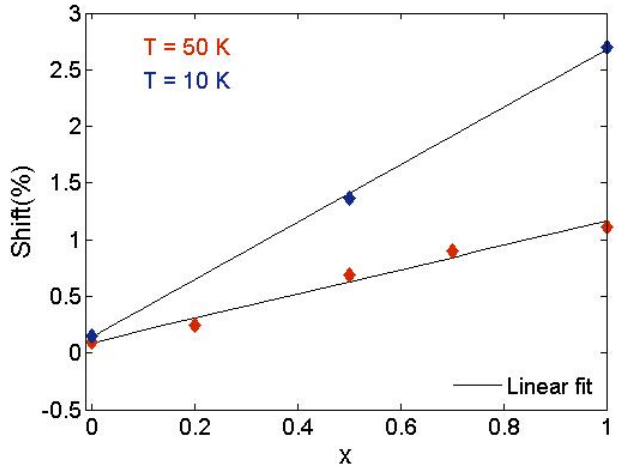

Figure 4.3: The relation between substitutional La-for-Ce level in the sample with iso shift at 10 K and 50 K. The solid lines represent a linear fit of the data.

As shown in Fig. 4.4, both NMR lines at two different temperature broaden upon increasing in the substitutional La-for-Ce level, with FWHM values changing smoothly from about 0.5 to 2.5 MHz for $T = 10$ K and from 0.5 to 1.8 MHz for $T = 50$ K.

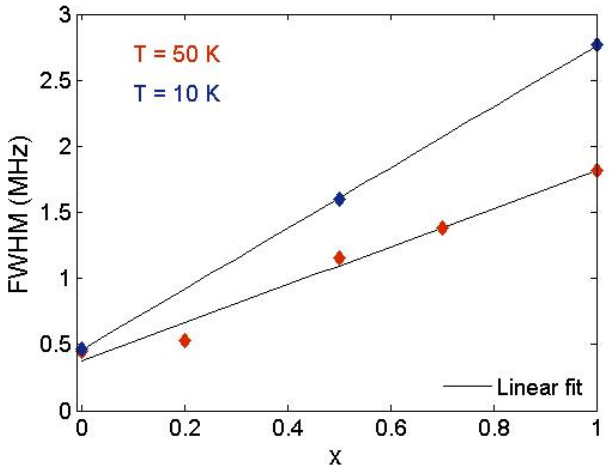

Figure 4.4: The relation between substitutional La-for-Ce level in the sample with FWHM. The solid lines represent a linear fit of the data.

4.2 Spin-Lattice Relaxation rate T_1^{-1}

As explained in Sec. 3.2.2 we have measured the spin-lattice relaxation time with an inversion recovery method and we have then fitted the experimental points. In the following, we report the results for $Ce_xLa_{1-x}NiGa_2$ series. In Fig. 4.5 we show an example of the nuclear magnetization recovery m(t) for $Ce_{0.5}La_{0.5}NiGa_2$ in B=5 T and temperature equal 50 K, used to evaluate the spin-lattice relaxation rates. The solid line represents fit to the data using the parameter function given in Eq. 2.39.

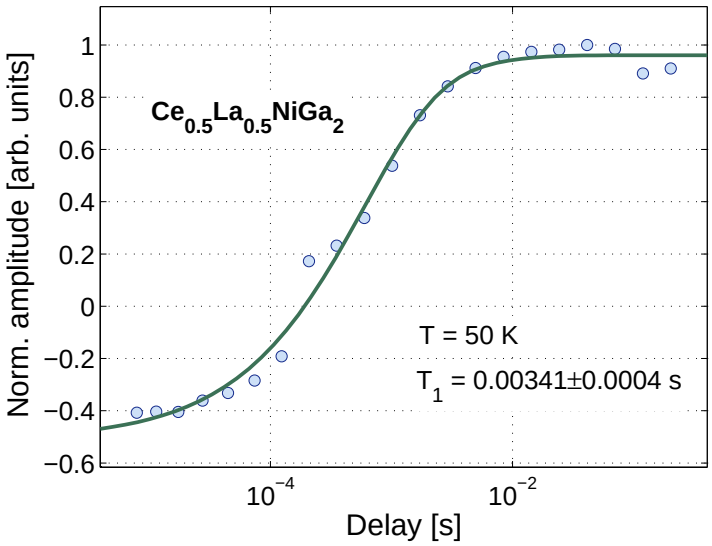

Figure 4.5: Nuclear magnetization recovery m(t) for $Ce_{0.5}La_{0.5}NiGa_2$ at T=50 K, ν=65.4 MHz and a field of 5 T , The solid line represents fit of the data .

In the case of the spin-lattice relaxation time, we can separate the contribution of f-electron from the mechanism of the non-interacting conduction electrons, via the formula,

$$\frac{1}{T_1} = \frac{1}{T_{10}}[1 + 2N(E_F)C] \tag{4.4}$$

where T_1 is the spin-lattice relaxation time of $CeNiGa_2$ and T_{10} is the same for $LaNiGa_2$, whereas f-electrons play no role and $N(E_F)$ is the density of states at the Fermi energy. In figure 4.6 we show T_1^{-1}(T) of $Ce_xLa_{1-x}NiGa_2$ series for various substitutional La-for-Ce level between 0.1 and 300 K on linear scale Fig. 4.6 (a) and logarithmic scale Fig. 4.5 (b). The spin-lattice relaxation rate $T_1^{-1}(T)$ of $LaNiGa_2$ follows a linear -in-T dependent with the value of $(T_1T)^{-1}$ is 0.6 (s K^{-1}), also for $Ce_{0.2}La_{0.8}NiGa_2$ it is look similar to $LaNiGa_2$.

A complete understanding of the nuclear spin-lattice relaxation rate in heavy-electron systems poses a formidable task. We first consider the spin-lattice relaxation in the paramagnetic phase, for the samples $Ce_xLa_{1-x}NiGa_2$ series with x $\geq$ 0.5 and in the temperature range $T > T_K$, $T_1^{-1}(T)$ is constant, and 0.330 $\pm$ 0.01 (s^{-1}) for $CeNiGa_2$. The values of the T_K and T_N for the samples are given in Table 4.1.

As we know, in paramgnetic state at high temperature limit the susceptibility

$\chi(T)$ is well described by a Curie-Weiss law of the form:

$$\chi(T) = \chi_0 + \frac{C}{T-\theta} \tag{4.5}$$

where χ_0 is the temperature-independent part to the susceptibility, C is the Curie constant and θ is the Curie-Weiss temperature. The Knight shift evaluated with the magnetic susceptibility as shown in Eq. 4.2, the spin-lattice relaxation rate will consist of two contributions:

$$\frac{1}{T_1} = \frac{1}{T_1^{Korringa}} + \frac{1}{T_1^{4f}} \tag{4.6}$$

For the second term, one finds:

$$\frac{1}{T_1^{4f}} \propto T\chi \cong const. \tag{4.7}$$

Table 4.1: Values of the T_K and T_N for $Ce_xLa_{1-x}NiGa_2$ when x ≥ 0.5.

Samples	T_K[K]	T_N[K]
$Ce_{0.5}La_{0.5}NiGa_2$	29.3 ± 0.6	0.2±0.2
$Ce_{0.7}La_{0.3}NiGa_2$	33.5± 1.2	1.8±0.3
$CeNiGa_2$	33.9 ± 0.8	3.5±0.2

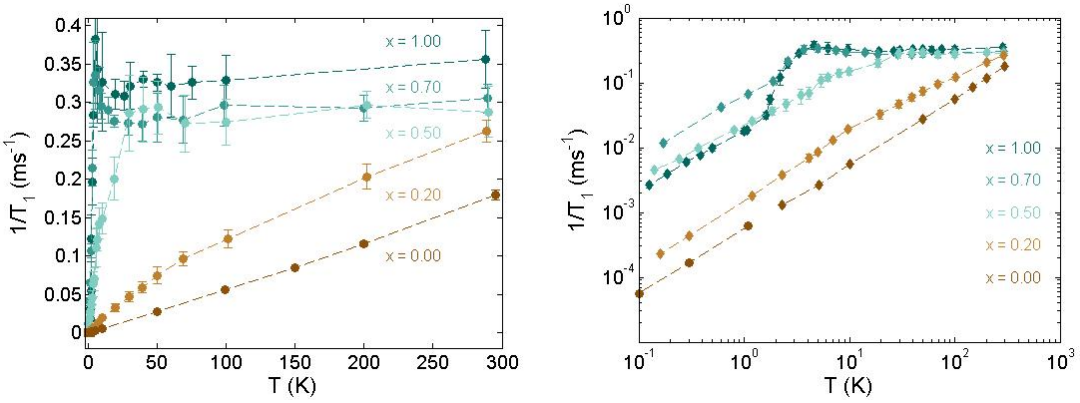

(a) (b)

Figure 4.6: Temperature dependent of T_1^{-1} for $Ce_xLa_{1-x}NiGa_2$ series measured for different values of cerium content x. The dashed lines are to guide the eye.

Turning to Fig. 4.6, we observe that for $Ce_{0.5}La_{0.5}NiGa_2$, when $T > T_K$ $T_1^{-1}(T)$ is constant with temperature and equal 0.286 ± 0.008 (s^{-1}), where the magnetic moment behave like free (paramagnetic moments). In the temperature range $T_K^* < T < T_K$, where is the Kondo phase 1, T_1^{-1} varies linearly with temperature as well as the kondo phase 2 is in the temperature range $T_N < T < T_K^*$, as shown in Fig. 4.7

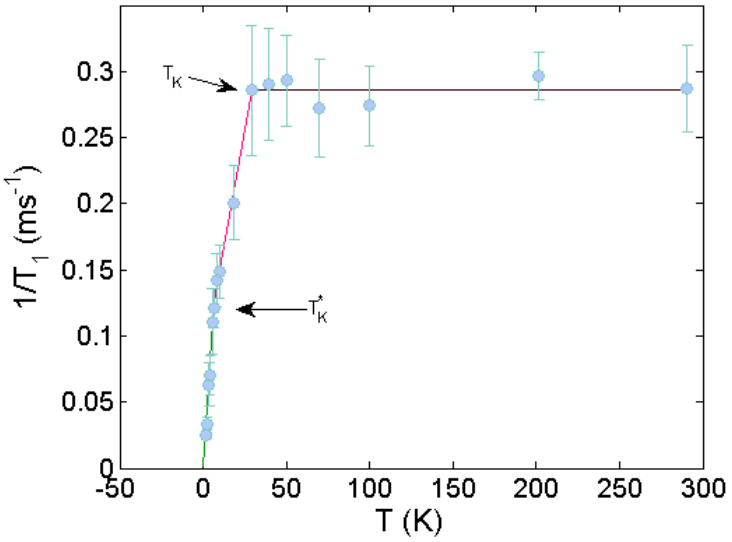

Figure 4.7: ^{71}Ga NMR $1/T_1$ relaxation rate vs. T for $Ce_{0.5}La_{0.5}NiGa_2$. Colors refer to different relaxation regimes. The solid line represents a linear fit of the data.

In Fig. 4.8 we present the result of the spin-lattice relaxation rate $T_1^{-1}(T)$ measurements for $Ce_{0.7}La_{0.3}NiGa_2$ in the temperature range between 100 mK and 300 K. In the high temperature regime, above T_K we observe that T_1^{-1} is constant with temperature and equal 0.285 ± 0.012 (s^{-1}), in the temperature range $T_K < T < T_N$ the curve starts growing with a moderate slope that gradually increases until at ∼ 5 K it is drastically augmented. On the lower temperature side of the peak, the curve decays steeply. In $T < T_N$ regime, T_1^{-1} varies linearly with temperature.

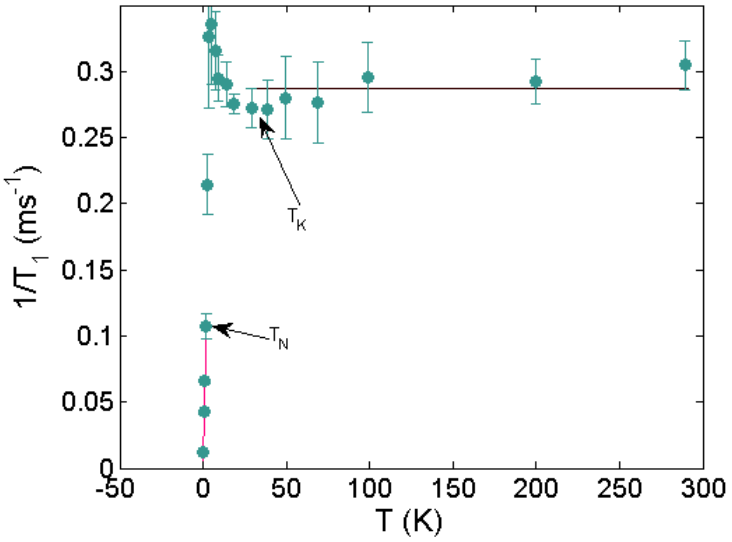

Figure 4.8: ^{71}Ga NMR $1/T_1$ relaxation rate vs. T for $Ce_{0.7}La_{0.3}NiGa_2$. Colors refer to different relaxation regimes. The solid line represents a linear fit of the data.

In Fig. 4.9 we present the result of the spin-lattice relaxation rate $T_1^{-1}(T)$ measurements for $CeNiGa_2$ in the temperature range between 100 mK and 300 K. In the

high temperature regime, above T_K we observe that T_1^{-1} is constant with temperature and equal 0.33 ± 0.01 (s^{-1}), in the temperature range $T_K < T < T_N$, the curve starts growing with a moderate slope that gradually increases until at ∼ 5 K it is drastically augmented. On the lower temperature side of the peak. In $T_N/2 < T < T_N$ regime, T_1^{-1} varies linearly with temperature equal 0.14 ± 0.03 [$s^{-1}K^{-1}$] T - 0.20 ± 0.09 [s^{-1}]. $T < T_N/2$, T_1^{-1} varies linearly with temperature equal 0.018 ± 0.001 [$s^{-1}K^{-1}$] T 1.0 ± 0.1 [s^{-1}].

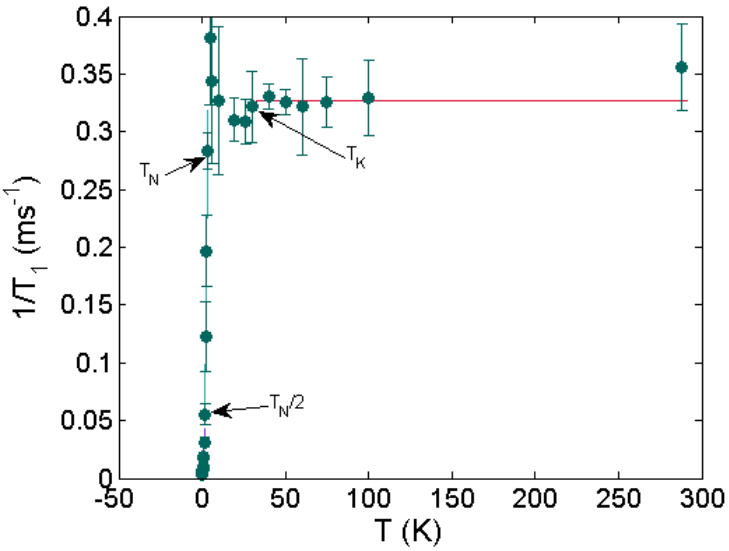

Figure 4.9: ^{71}Ga NMR $1/T_1$ relaxation rate vs. T for $CeNiGa_2$. Colors refer to different relaxation regimes. The solid line represents a linear fit of the data.

Figure 4.10 displays the Korringa's product $(T_1T)^{-1}$ as a function of temperature, for our five samples on logarithmic scales. We had discussed in Sec. 2.3.1 that in isotropic, paramagnetic materials the former quantity is found to be constant. What we have found, is that, for $LaNiGa_2$, this quantity is constant, such as $Ce_{0.2}La_{0.8}NiGa_2$ below 9.7 K. For $Ce_{0.5}La_{0.5}NiGa_2$, above 5.4 K, T_1^{-1} is thermally independent, as well below 5.4 K, T_1^{-1} varies approximately linearly with temperature.In the same figure, the functional form of $(T_1T)^{-1}(T)$ for $Ce_{0.7}La_{0.3}NiGa_2$ and $CeNiGa_2$ are quite complicated, for $Ce_{0.7}La_{0.3}NiGa_2$ above 3.7 K, T_1^{-1} is temperature independent, below 3.7 K, $(T_1T)^{-1}$ first decreases by an order of magnitude but below 1.9 K the Korringa-type of T dependence of the relaxation rate is observed. In $CeNiGa_2$, above 4.6 K, T_1^{-1} is temperature independent, below T_N =3.5 K, $(T_1T)^{-1}$ first decreases by an order of magnitude but below 1.6 K the Korringa-type of T dependence of the relaxation rate is observed with $(T_1T)^{-1}$ one order of magnitude smaller than the corresponding values for $Ce_{0.5}La_{0.5}NiGa_2$ and $Ce_{0.7}La_{0.3}NiGa_2$

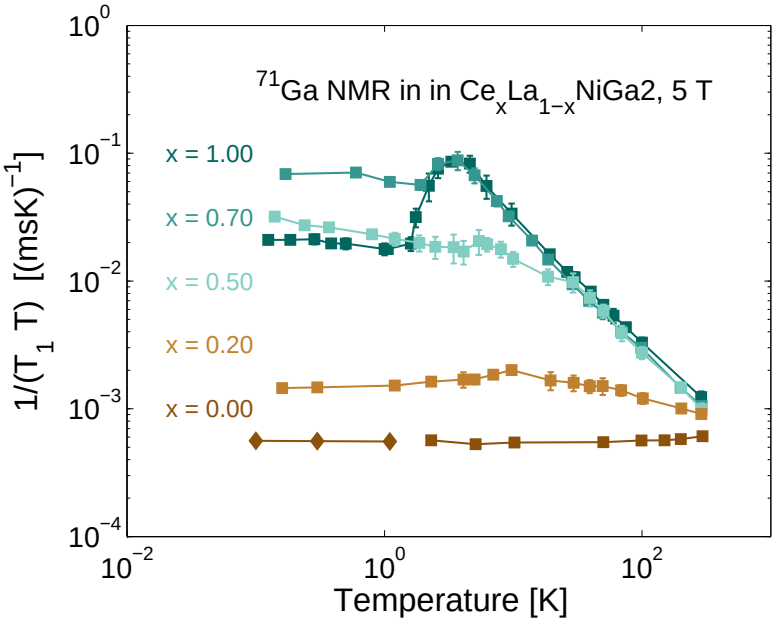

Figure 4.10: Temperature dependence of $(T_1T)^{-1}$ for $Ce_xLa_{1-x}NiGa_2$ series with x equal 0, 0.2, 0.5, 0.7 and 1. The solid lines are to guide the eye.

In Fig 4.11 we confirm the relation between substitutional La-for-Ce level of the samples and temperatures. When the temperature is greater than T_K, a paramagnetic phyase is observed. In intermediate values of temperature between T_K and T_N, the system tends to heavy fermion behavior (the Kondo effect is dominant). When temperature is smaller than T_N, then, the system has an antiferromagnetic ground state (the RKKY interaction is dominant).

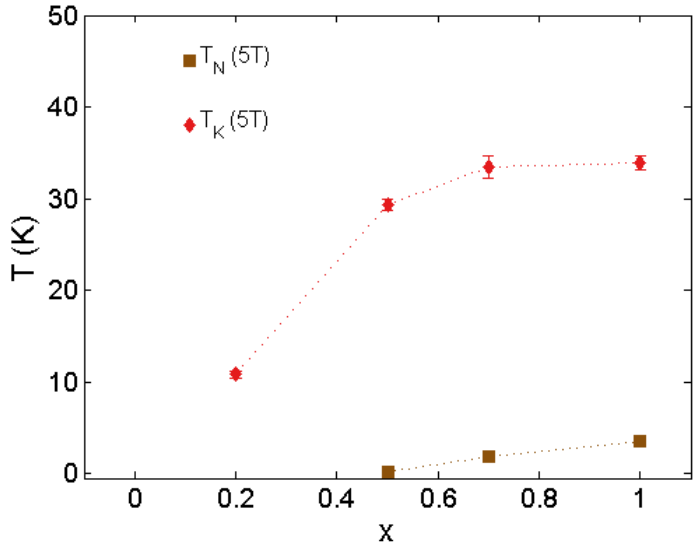

Figure 4.11: The relation between substitutional La-for-Ce level in the sample with temperature for $Ce_xLa_{1-x}NiGa_2$ series. The dash lines are to guide the eye, which divides the three regions of the phase diagram.

4.2.1 Comments on the Korringa ratio

In our samples belonging to the $Ce_xLa_{1-x}NiGa_2$ series, we find a linear variation of $1/T_1$(T) for $LaNiGa_2$, the value of T_1T being 1.66 s·K, by considering the measured 0.13% Knight shift, therefore, the experimental Korringa constant (see Eq. 4.8) is 3.03×10^{-6} s·K where the theoretical value for all samples is 2.8156×10^{-6} s·K (see Eq. 4.9). The Korringa ratio $\alpha = 0.926 \sim 1$ reflects the behavior of a Fermi gas (normal metal without correlations). For $Ce_{0.2}La_{0.8}NiGa_2$, we find a linear variation of $1/T_1$(T) when T < 70 K, the value of T_1T is 1.19 sK, by considering the measured 0.04% Knight shift, therefore, the experimental Korringa constant is 2.2×10^{-7} s·K (see Eq. 4.8). From the relative Korringa ratio $\alpha = 12.69 \gg 1$, as well as α for $Ce_{0.5}La_{0.5}NiGa_2$ and $Ce_{0.7}La_{0.3}NiGa_2$ are much grater than 1 (see table 4.2), so maybe the Korringa model is not suitable in these cases. For $CeNiGa_2$ the Korringa ratio α= 0.46 $\sim$ 0.5 indicates that the observed system exhibits anitferromagnetic correlations.

Experimental Korringa constant:

$$S_{exp} = T_1 T K^2 \tag{4.8}$$

Theoretical Korringa value:

$$S_0 = \hbar(\gamma_e/\gamma_{Ga})^2/(4\pi k_B) = 2.8156 \times 10^{-6}\,\text{s}\cdot\text{K} \tag{4.9}$$

Korringa ratio:

$$\alpha = S_0/S_{exp} \tag{4.10}$$

Table 4.2: Data show the relation between the Korringa ratio and x.

S_{exp}	3.0374e-6	2.2175e-7	8.5834e-7	7.6007e-7	6.0784e-6
α	0.92698	12.697	3.2803	3.7044	0.46322
x	0	0.2	0.5	0.7	1

4.3 Spin-Spin relaxation rate T_2^{-1}

We have performed measurements of the spin-spin relaxation rate, T_2^{-1} measured in an applied magnetic field B= 5 T at a frequency ν=65.4 MHz in the temperature range between 100 mK and 300 K, for $Ce_xLa_{1-x}NiGa_2$ series with $x = 0.2$, 0.5 and 0.7, as shown in Fig. 4.12. In the high-temperature regime, above T_K, T_2^{-1} is constant with temperature. For temperatures around T_K there is an upturn in all the samples (epitomized by the loss of coherence),in the low temperature regime.

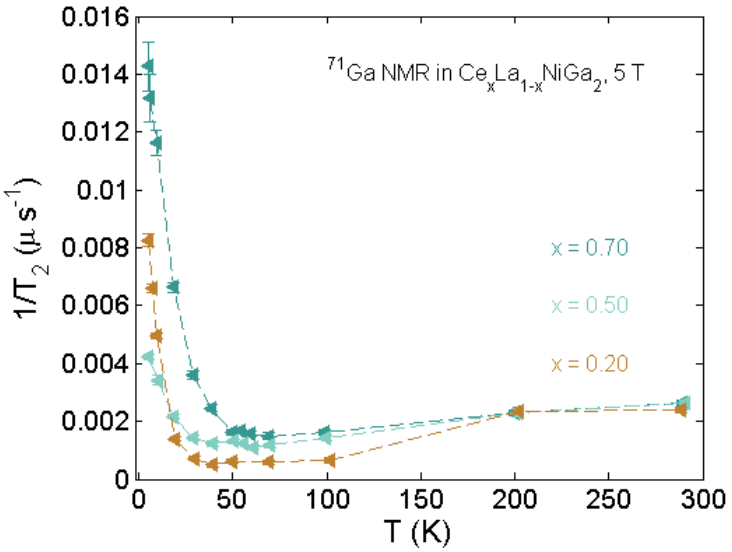

Figure 4.12: Temperature dependence of T_2^{-1} measured in applied magnetic field B= 5 T at a frequency ν=65.4 MHz, for $Ce_xLa_{1-x}NiGa_2$ series with x equal 0.2, 0.5 and 0.7. The dashed lines are a guide to the eye.

Chapter 5

Conclusions

In this study we performed NMR measurements on five different compounds belonging to the family of $Ce_xLa_{1-x}NiGa_2$ series. The five x-values we chose to investigate were 0, 0.2, 0.5, 0.7 and 1. As a probing nucleus, we chose ^{71}Ga. For each material, we performed measurements on a powder samples.

The transverse relaxation time of these materials was rather long, so that it allowed us to apply a standard spin-echo sequence, with delays of $\sim 100\ \mu s$. The measurements were performed in a temperature range going from room temperature down to below liquid-helium temperature. Under normal conditions our cooling system allowed us to reach ~ 4 K, but occasionally, by means of pumping, we could reach 2 K.

In particular, we investigated how the shift and the shape of ^{71}Ga NMR lines evolve with the substitutional La-for-Ce level. We studied the variations with temperature of the longitudinal relaxation processes of the ^{71}Ga nuclear magnetization too. We have shown that the substitutional La-for-Ce level strongly affects the spin-lattice relaxation rate of $Ce_xLa_{x-1}NiGa_2$ series at x-values $= 0.5$, 0.7 and 1. In substitution of La-for-Ce level between 0.5 and 1, and below T_K, the nuclear spin-lattice relaxation is only slightly enhanced compared to the corresponding values for $LaNiGa_2$, similar to what is observed at much higher temperatures.

Bibliography

[1] Z. Fisk and H. R. Ott. Superconductivity in new materials. In E. Burstein, M. L. Cohen, D. L. Mills, and P. J. Stiles, editors, *Contemporary concepts of condensed matter science*, volume 4. Elsevier, Oxford, UK, 2010.

[2] J. M. Hollas. *Modern spectroscopy*. John Wiley & Sons, Chichester, UK, 2004.

[3] V. Zlatic and A. Hewson. *Properties and applications of thermoelectric materials: the search for new materials for thermoelectric devices*. Springer Science & Business Media, Berlin, 2009.

[4] R. J. Elliott. Crystal field theory in the rare earths. *Reviews of Modern Physics*, 25(1):167, 1953.

[5] F. Casola. *Aspects of quantum magnetism in quasi one-dimensional materials: An NMR study*. PhD thesis, ETH Zurich, 2013.

[6] S. Blundell. Magnetism in condensed matter, 2003.

[7] J. Nygård, D. H. Cobden, and P. E. Lindelof. Kondo physics in carbon nanotubes. *Nature*, 408(6810):342, 2000.

[8] M. Weller. *NMR/NQR studies at very low temperatures and high pressures in strongly correlated electron systems*. PhD thesis, ETH Zurich, 2007.

[9] B. Coqblin, J. R. Iglesias, N. B. Perkins, S. G. Magalhaes, and F. M. Zimmer. Doniach diagram for ordered, disordered and underscreened Kondo lattices. *Journal of Magnetism and Magnetic Materials*, 320(14):1989–1994, 2008.

[10] A. C. Hewson. *The Kondo problem to heavy fermions*, volume 2. Cambridge university press, Cambridge, UK, 1997.

[11] L. Kouwenhoven and L. Glazman. Revival of the Kondo effect. *Physics world*, 14(1):33, 2001.

[12] José Luiz Ferreira da Silva Jr. *Theory of lanthanide systems: valence transitions and interplay of Kondo effect and disorder*. PhD thesis, Université Grenoble Alpes, 2016.

[13] J. Kroha. Interplay of Kondo effect and RKKY interaction. *arXiv preprint arXiv:1710.00192*, 2017.

[14] J. G. Soldevilla, J. C. Sal, J. A. Blanco, J. I. Espeso, and J. R. Fernández. Phase diagram of the $CeNi_{1-x}Cu_x$Kondo system with spin-glass-like behavior favored by hybridization. *Physical Review B*, 61(10):6821, 2000.

[15] O. O. Bernal, D. E. MacLaughlin, H. G. Lukefahr, and B. Andraka. Copper NMR and thermodynamics of $UCu_{5-x}Pd_x$: evidence for kondo disorder. *Physical review letters*, 75(10):2023, 1995.

[16] M. H. Levitt. *Spin dynamics: basics of nuclear magnetic resonance*. John Wiley & Sons, Chichester, UK, 2001.

[17] O. Zerbe and S. Jurt. *Applied NMR spectroscopy for chemists and life scientists*. John Wiley & Sons, Chichester, UK, 2013.

[18] B. Cowan. *Nuclear Magnetic Resonance and Relaxation*. Cambridge University Press, Cambridge, UK, 1997.

[19] M. Vachon. *Nuclear Magnetic Resonance Study of the Magnetism in the 2D Frustrated Quantum Heisenberg Antiferromagnet Cs_2CuCl_4*. PhD thesis, Brown University, 2009.

[20] F. Hammerath. *Magnetism and Superconductivity in Iron-based Superconductors as Probed by Nuclear Magnetic Resonance*. Springer Science & Business Media, 2012.

[21] A. Abragam and A. Abragam. *The principles of nuclear magnetism*. Number 32. Oxford university press, Oxford, UK, 1961.

[22] Pascal P Man. Quadrupolar interactions. *EMagRes*, 2007.

[23] V. Chlan, P. Dolezal, R. Sgallova, C. Franz, and P. Javorsky. Local atomic arrangement in $LaCuAl_3$ and $LaAuAl_3$ by NMR and density functional theory. *arXiv preprint arXiv:1811.02871*, 2018.

[24] M. H. Cohen and F. Reif. Quadrupole effects in nuclear magnetic resonance studies of solids. In F. Seitz and D. Turnbull, editors, *Solid state physics*, volume 5, pages 321–438. Academic Press, New York, 1957.

[25] B. S. Shastry and E. Abrahams. What does the Korringa ratio measure? *Physical Review Letters*, 72(12):1933, 1994.

[26] J. Keeler. *Understanding NMR Spectroscopy*. John Wiley & Sons, Chichester, UK, 2010.

[27] J. Cui. Studies of energy-relevant materials by nuclear magnetic resonance. 2017.

[28] P. Matus. Influence of local C_{60} orientation on electronic properties of A_3C_{60} compounds. 2006.

[29] P. Vonlanthen, J. L. Gavilano, B. Ambrosini, D. Heisenberg, F. Hulliger, and H.-R. Ott. Nuclear magnetic resonance studies of $CePd_2In$ and $LaPd_2In$ at low temperatures. *Zeitschrift für Physik B Condensed Matter*, 102(3):347–357, 1997.

[30] Y. Aoki, K. Terayama, and H. Sato. Magnetic, thermal and transport properties of $CeNiGa_2$. *J. Phys. Soc. Jpn.*, 64(10):3986–3992, 1995.